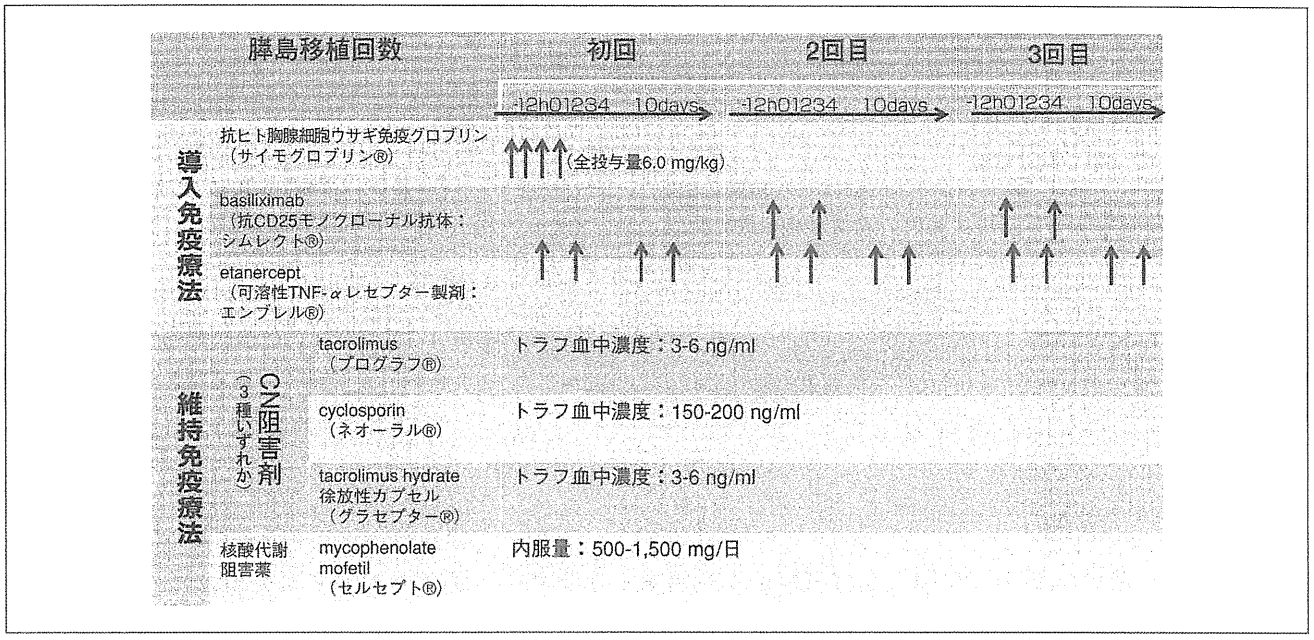

図7　膵島移植臨床試験の免疫抑制プロトコール

設した高度医療評価制度に申請，承認された。本制度の承認により，原則として保険との併用が認められていない医薬品・医療機器の使用を，先進医療の一類型として保険診療と併用することが可能となる。今後の薬事法上の申請につながるデータ収集を図るため，臨床試験推進拠点（東北大学病院臨床試験推進センターおよび先進医療振興財団）の支援を得て質の高い臨床試験体制が整備されている。

この臨床試験は2011年2月に実施施設の施設登録が開始され，その後，候補者に対する登録前検査の実施，コーディネーション体制の構築等が行われ，2012年6月より臨床膵島移植が再開となった。2012年6月から9月までに，2件の心停止ドナーからの膵提供があり膵島分離を施行したが，移植基準を満たさず移植には至っていない。

IV. 今後の展望

改正臓器移植法施行後，脳死下臓器提供数が増加した一方，脳死下に提供可能であった膵臓が，何らかの医学的理由により膵臓移植に用いることができない場合も散見されるようになった。これを受けて，膵臓移植に用いられない膵臓で，膵島移植には用いることができると判断された場合の膵臓を膵島移植に利用する体制が構築されてきている。先進医療の範疇であっても脳死下提供膵を用いることができるよう，再度高度医療評価会議での審議を受け承認された。先進医療専門家会議を経て，年内には脳死下提供膵から分離された膵島もこの臨床試験に用いることが可能になる見込みである。膵島移植が組織移植の範疇に分類されていることで複雑化しうるコーディネーション体制においては，人員の不足や連携体制などに課題が多い。また，移植の基準を満たさないヒト分離膵島の研究転用体制の構築も求められており，これらの課題について，日本膵・膵島移植研究会内や関係各所との間で検討が進められている。

V. おわりに

日本膵・膵島移植研究会が，膵島移植を1型糖尿病のひとつの治療選択肢として確立するために取り組んできたこれまでの過程を誌上で公にすることができた。日本膵・膵島移植研究会会員をはじめとする関係各位に対し，稿を終えるにあたり改めて感謝の意を表したい。

文責：日本膵・膵島移植研究会膵島移植班事務局
穴澤貴行，後藤満一

文　献

1）穴澤貴行，後藤満一．膵島移植の現況．膵臓 2011; 26: 169-175.

2）膵・膵島移植研究会編. 膵島移植実施マニュアル第3版. 東京: 膵島移植研究会, 2006.
3）Shapiro AM, Ricordi C, Hering BJ, *et al.* I International trial of the Edmonton protocol for islet transplantation. N Engl J Med 2006; 355: 1318-1330.
4）O'Gorman D, Kin T, Imes S, *et al.* Comparison of human islet isolation outcomes using a new mammalian tissue-free enzyme versus collagenase NB-1. Transplantation 2010; 90: 255-259.
5）Hering BJ, Kandaswamy R, Ansite JD, *et al.* Single-donor, marginal-dose islet transplantation in patients with type 1 diabetes. JAMA 2005; 293: 830-835.

OPEN ACCESS Freely available online

PLOS | ONE

Tacrolimus Inhibits the Revascularization of Isolated Pancreatic Islets

Ryuichi Nishimura[1], Sho Nishioka[2], Ikuma Fujisawa[2], Hitoshi Shiku[2], Miki Shimada[3], Satoshi Sekiguchi[1], Keisei Fujimori[1], Akira Ushiyama[4], Tomokazu Matsue[5], Noriaki Ohuchi[1], Susumu Satomi[1], Masafumi Goto[1,6]*

1 Division of Advanced Surgical Science and Technology, Tohoku University, Sendai, Japan, **2** Graduate School of Environmental Studies, Tohoku University, Sendai, Japan, **3** Department of Pharmaceutical Sciences, Tohoku University Hospital, Sendai, Japan, **4** Department of Environmental Health, National Institute of Public Health, Wako, Japan, **5** WorldPremier InternationalResearch Center Initiative Advanced Institute for Materials Research, Tohoku University, Sendai, Japan, **6** New Industry Creation Hatchery Center, Tohoku University, Sendai, Japan

Abstract

Aims: Immunosuppressive drugs could be crucial factors for a poor outcome after islet allotransplantation. Unlike rapamycin, the effects of tacrolimus, the current standard immunosuppressant used in islet transplantation, on graft revascularization remain unclear. We examined the effects of tacrolimus on islet revascularization using a highly sensitive imaging system, and analyzed the gene expression in transplanted islets by introducing laser microdissection techniques.

Methods: Islets isolated from C57BL/6-Tg (CAG-EGFP) mice were transplanted into the nonmetallic dorsal skinfold chamber on the recipients. Balb/c athymic mice were used as recipients and were divided into two groups: including a control group (n = 9) and tacrolimus-treated group (n = 7). The changes in the newly-formed vessels surrounding the islet grafts were imaged and semi-quantified using multi-photon laser-scanning microscopy and a Volocity system. Gene expression in transplanted islets was analyzed by the BioMark dynamic system.

Results: The revascularization process was completed within 14 days after pancreatic islet transplantation at subcutaneous sites. The newly-formed vascular volume surrounding the transplanted islets in the tacrolimus-treated group was significantly less than that in the control group ($p<0.05$). Although the expression of *Vegfa* ($p<0.05$) and *Ccnd1* ($p<0.05$) was significantly upregulated in the tacrolimus-treated group compared with that of the control group, no differences were observed between the groups in terms of other types of gene expression.

Conclusions: The present study demonstrates that tacrolimus inhibits the revascularization of isolated pancreatic islets without affecting the characteristics of the transplanted grafts. Further refinements of this immunosuppressive regimen, especially regarding the revascularization of islet grafts, could improve the outcome of islet allotransplantation.

Citation: Nishimura R, Nishioka S, Fujisawa I, Shiku H, Shimada M, et al. (2013) Tacrolimus Inhibits the Revascularization of Isolated Pancreatic Islets. PLoS ONE 8(4): e56799. doi:10.1371/journal.pone.0056799

Editor: Kathrin Maedler, University of Bremen, Germany

Received July 23, 2012; **Accepted** January 16, 2013; **Published** April 17, 2013

Copyright: © 2013 Nishimura et al. This is an open-access article distributed under the terms of the Creative Commons Attribution License, which permits unrestricted use, distribution, and reproduction in any medium, provided the original author and source are credited.

Funding: This study has been supported by grants from the Japanese Grant-in-Aid for Scientific Research (B), the Takeda Science Foundation, the Mochida Memorial Foundation for Medical and Pharmaceutical Research, and the Japanese Ministry of Health, Welfare and Labor (20120101). The funders had no role in study design, data collection and analysis, decision to publish, or preparation of the manuscript.

Competing Interests: The authors have declared that no competing interests exist.

* E-mail: gotokichi@aol.com

Introduction

Pancreatic islet transplantation is an emerging and promising therapy for type 1 diabetes. However, at least two donor pancreata are needed to reverse hyperglycemia, and substantial number of islet grafts fail within 5 years [1]. Although several factors may contribute to a progressive decline in the function of islet transplants, the main reason for this problem is still uncertain. Pancreatic islet autotransplantation, despite the use of a lower beta-cell mass, shows good results and improves insulin-independence rates in comparison to the islet allotransplantation [2]. Pancreatic islet allografts are affected by various factors, including relatively long cold ischemia times before pancreatic islet isolation [3,4], the need for a purification procedure, and the use of immunosuppressive drugs to regulate the alloimmune responses to the islet grafts.

The inhibitory effects of rapamycin, a key component of the immunosuppressive regimen in the Edmonton protocol, on tumor angiogenesis or pancreatic islet revascularization have recently been clarified [5,6,7,8,9]. However, the inhibitory effects of tacrolimus, which is one of the standard immunosuppressants in both pancreatic islet transplantation and whole pancreas transplantation, on revascularization has been poorly studied, although Turgut et al. reported the prevention of corneal neovascularization by the systemic and topical administration of tacrolimus [10].

Therefore, this study sought to evaluate the effect of tacrolimus on the islet revascularization process using a highly sensitive imaging system combined with the dorsal skinfold chamber (DSC)

technique and multi-photon laser-scanning microscopy (MPLSM). This new system enabled repeated observation of the time-dependent changes of islet grafts and surrounding vessels in identical animals without histological sectioning [11]. Spier et al. introduced the anterior chamber of the eye for monitoring revascularization of the islet grafts by using MPLSM [12,13]. Although the anterior chamber of the eye is a breakthrough model, it is not realistic for clinical application. In contrast, the subcutaneous space is an ideal site for islet transplantation due to the minimal invasion and easy access. The liver, which is the current standard transplant site, is often associated with procedure-related complications including hemorrhage, thrombosis, and the strong innate immune response such as the instant blood-mediated inflammatory reaction (IBMIR) [14,15], thus the current model could be a useful and practical tool to analyze the revascularization process of islet grafts.

Hence, the present study examined the effect of tacrolimus on islet revascularization using a highly sensitive imaging system. Furthermore, this study attempted to analyze the state of gene expression in transplanted islet grafts *per se* by introducing laser microdissection techniques.

Materials and Methods

Mouse models

All animals used in this study were handled in accordance with the Guide for the Care and Use of Laboratory Animals published by the National Institutes of Health [16]. The animal studies were approved by the Animal Care and Use Committee of the Tohoku University (approved protocol ID: 2011 NICHe-Animal-13). All surgeries were performed under anesthesia, and all efforts were made to minimize suffering. Male C57BL/6-Tg (CAG-EGFP) mice (9–12 weeks of age; Japan SLC Inc., Shizuoka, Japan) were used as islet donors.

The dorsal skinfold chamber (DSC), which is composed of polyacetal resin (generally known as Duracon; grade M90-44, Polyplastics Co.,Ltd., Tokyo, Japan) [17], was introduced into the recipient mice [11] (Fig. 1A). This nonmetallic chamber is approximately 40% lighter in weight than metallic chamber used traditionally, subjecting mice to less stress. DSC was implanted into male Balb/c nu/nu mice (8–12 weeks of age; Japan SLC Inc.). This model, unlike wild type Balb/c mice, allowed observation for a relatively long preservation period and also to focus on the influence of immunosuppressive chemicals on engraftment without any interference from the specific immune responses.

All animals were bred and maintained in a pathogen-free environment with free access to laboratory chow and water and exhibited no signs of discomfort.

Pancreatic islet isolation and culture

C57BL/6-Tg (CAG-EGFP) mice were anesthetized with the inhalation of isoflurane (Abbott Japan Co., Ltd., Tokyo, Japan). The bile duct was identified and clamped at the papilla Vateri. Four milliliters of cold Hank's balanced salt solution (HBSS) containing 1 g/L collagenase (Sigma type V; Sigma Chemicals, St. Louis, MO, USA) was injected into the common bile duct leading to the pancreas under a stereomicroscope. The pancreas was removed and incubated in a water bath at 37°C for 16 min. The pancreas was digested, the cell suspension was washed two times in HBSS and centrifuged for 1 min. Density-gradient centrifugation was performed for 10 min using Histopaque-1119 (Sigma Diagnostics, St. Louis, MO, USA) and Lymphoprep™ (Nycomed Pharma AS, Oslo, Norway) to isolate pancreatic islets. The islets were cultured in RPMI-1640 containing 5.5 mmol/L glucose and 10% fetal bovine serum at 37°C in 5% CO_2 and humidified air for approximately 3 hours before examination.

Islet transplantation into the dorsal skinfold chamber

Balb/c nu/nu mice underwent islet transplantation into the DSC under isoflurane (Abbott Japan Co., Ltd.) anesthesia. Two to ten of isolated islets were transplanted into each DSC by means of the hand-picking method. The space between skin flap and the cover glass was filled with saline to remove air bubbles. The recovery rate of the grafts at the end of the observation period was almost same between the tacrolimus and control groups.

Experimental groups

The recipient mice with transplanted pancreatic islets were divided into two groups: the control group (n = 9) and the tacrolimus (Astellas, Deerfield, IL)-treated group (0.5 mg/kg/day; n = 7, two of seven islets were observed up to 11 days after transplantation due to technical trouble of DSC.) [18]. Tacrolimus was administered to mice via subcutaneous implanted MICRO-OSMOTIC PUMP (Model 1002, Alzet, Cupertino, CA) for 14 days. The control mice were also implanted with a MICRO-OSMOTIC PUMP and treated with vehicle.

Measurement of tacrolimus concentrations in the whole blood

Blood samples were obtained via the inferior vena cava at 7 days after the initial administration of tacrolimus. Blood samples were stored at −80°C until use. Tacrolimus concentrations in the whole blood were measured by using Dimension TACRO (Siemens Healthcare Diagnostics, Inc., Newark, DE, USA).

In vivo imaging of islets transplanted into the dorsal skinfold chamber

A 0.1 mL sample of Texas Red (10 mg/mL; Invitrogen, Leek, The Netherlands) was injected intravenously via the tail vein. The mice were anesthetized using the inhalation of isoflurane and then were positioned in an acrylic resin tube with an inner diameter of 26 mm. The tube was fixed on an acrylic resin plate and then placed on the microscope stage (Fig. 1B). A multiphoton laser-scanning microscope (MPLSM; FluoView FV1000MPE; OLYMPUS, Tokyo, Japan) equipped with water-dipping lenses (OLYMPUS XLPLN25XWMP NA1.05; OLYMPUS) was used to image the transplanted islet grafts. Distilled water was used as immersion liquid. MPLSM imaging was performed under the minimum required laser-power and scan-time necessary. No signs of photo-damage in islet cells or blood vessels were observed throughout the whole study. I processed images and measured newly-formed vascular volume surrounding the islets using a Volocity 3D system (PerkinElmer, Waltham, MA, USA) to evaluate islet revascularization. The newly-formed vascular volume surrounding the islets at each time point was calculated by the increasing rate against day 1 after transplantation. GFP and Texas Red were excited at 890 nm and separated and collected emission light onto two non-descanned detectors using a dichroic mirror (FV10-MRG/R:DM570) and emission filters (FV10-MRG/R:BA495-540HQ and BA575-630) [12,13].

Laser microdissection

The samples were divided into three groups: 1) islets before transplantation(n = 6), 2) islets in the control group(n = 6), 3) islets in the tacrolimus-treated group(n = 6). Tissues containing pancreatic islets, except for pancreatic islets before transplantation,

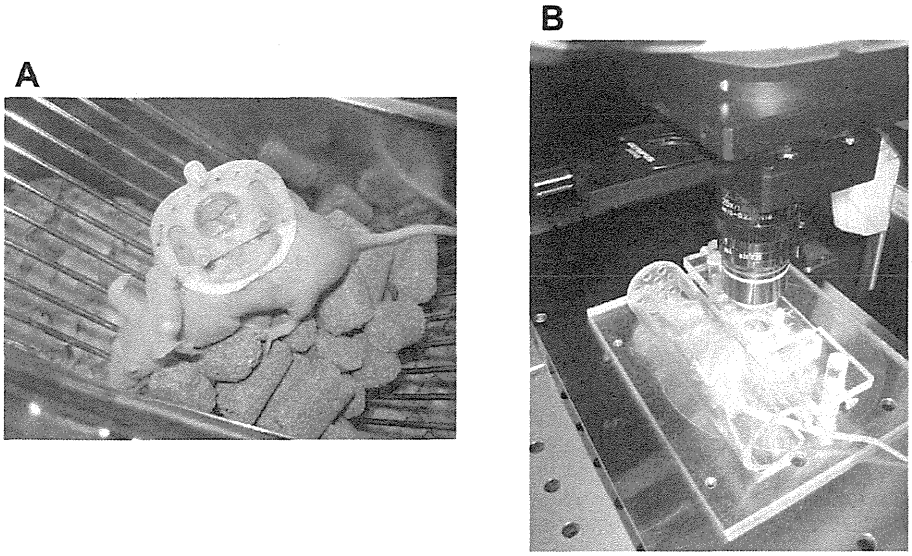

Figure 1. Mice bearing the dorsal skinfold chamber (A). Mice during microscopic observation (B). The mice were positioned in an acrylic resin tube during microscopic observation. The tube was fixed on an acrylic resin plate and then placed on the microscope stage.
doi:10.1371/journal.pone.0056799.g001

were harvested at 7 days after transplantation, frozen with liquid nitrogen and stored at −80°C until use. Ten μm frozen sections were prepared from each of these samples. Frozen prepared sections were fixed with acetone for 30 seconds, and then dehydrated and air dried immediately before performing laser microdissection (LMD). LMD was performed using LMD 7000 (Leica, Bensheim, Germany). The cell lysate was added, and the tube containing the micro-dissected islets was frozen with liquid nitrogen and stored at −80°C.

Quantitative real-time PCR analysis

The total RNA was extracted using the RNeasy Micro Kit (Qiagen, Tokyo, Japan) according to the manufacturer's protocol. The reverse transcription reaction was carried out to synthesize first strand cDNA according to the protocols for the QuantiTect Reverse Transcription kit (Qiagen) at 42°C for 30 min (RT reaction) followed by 95°C for 3 min (deactivation of RTase). The synthesized cDNA samples were stored at −30°C.

Gene expression was analyzed using the BioMark 48.48 dynamic gene expression system (Fluidigm, South San Francisco, CA, USA). Preamplified cDNA was diluted with RNase-free water (1:5) and used for quantitative PCR array analysis. A total of 33 genes were analyzed by the use of BioMark Real-Time PCR Analysis Software Version 2.0 (Fluidigm; Table S1). Actin, cytoplasmic 1 (Beta-actin) (*Actb*) was used as housekeeping gene.

Statistical analyses

All data are expressed as the means ± SEM. Statistical significance was determined using Student's *t*-test, or a one- and two-factor analysis of variance (ANOVA). The Bonferroni correction was used as a post-hoc test when the data were determined to be significant by ANOVA. *P* values less than 0.05 was considered to be significant.

Results

The time-dependent changes of newly-formed vascular volume surrounding the islets

Capillary sprout formation made an appearance at 4 days after transplantation, and these sprouts were interconnected at day 7. The newly-formed microvascular network gradually got bigger. The newly-formed vascular volume surrounding the islet grafts increased until Day 14, and subsequently reached a growth plateau (Figs. 2 and 3).

Tacrolimus concentrations in the whole blood

The blood concentrations of tacrolimus in the tacrolimus-treated group were 7.9±0.4 ng/mL (n = 6).

Inhibition of islet revascularization by administration of tacrolimus

The newly-formed vascular volume surrounding the transplanted islets in the tacrolimus-treated group was less than that in the control group (Fig. 3, $p<0.05$; Fig. 4). The increasing rate of newly-formed vascular volume surrounding the islets on day 14 was also significantly higher in the control group than in the tacrolimus-treated group ($p<0.05$; Fig. 5). The blood glucose levels in tacrolimus-treated group were maintained normoglycemic during the whole study period.

The time-dependent changes of islet graft volume

The islet graft volume was almost identical throughout the whole study period in both groups (Fig. 6).

Gene expression in the transplanted islets

The expression of 33 genes related to inflammation, metabolism, cell cycle, and angiogenesis in the transplanted islets was analyzed. In comparison to the islets before transplantation, the expression of vascular endothelial growth factor A (*Vegfa*) ($p<0.01$), mitogen-activated protein kinase 14 (*Mapk14*) ($p<0.05$), tissue factor (*F3*) ($p<0.01$), G1/S-specific cyclin-D1 (*Ccnd1*), and cell

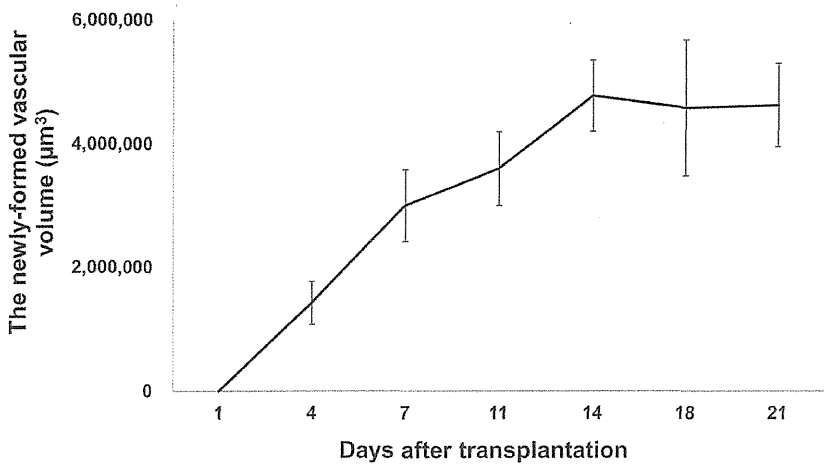

Figure 2. The time-dependent changes of newly-formed vascular volume for the transplanted pancreatic islets. Newly-formed vascular volume surrounding the islets at 4, 7, 11, 14, 18, and 21 days after transplantation was measured by using a Volocity system. All values are expressed as the means ± SEM.
doi:10.1371/journal.pone.0056799.g002

division protein kinase 4 (*Cdk4*) ($p<0.01$) was suppressed in the transplanted islet grafts (control group) (Fig. 6). In contrast, the expression of matrix metalloproteinase-14 (*Mmp14*) ($p<0.01$) was upregulated in the transplanted islet grafts. Although the expression of *Vegfa* ($p<0.05$) and Ccnd1 ($p<0.05$) was significantly upregulated in the tacrolimus-treated group compared with that of the control group, no differences were observed between the tacrolimus-treated and control groups in terms of other types of gene expression (Fig. 7).

Discussion

The outcome of islet allotransplantation is still far inferior to that of islet autotransplantation [2], despite the recent dramatic technical progress in the isolation of islets [3,19,20,21]. Although several factors might contribute to this issue, the use of immunosuppressive drugs in islet allotransplantation could be one of the crucial factors. Tacrolimus is thought to have only marginal adverse effects on islet grafts, and consequently is used as the standard drug in both pancreatic islet and whole pancreas transplantation [22,23]. Unlike whole pancreas transplantation, islet grafts are rendered avascular after enzymatic isolation and must become revascularized after pancreatic islet transplantation. However, the effects of tacrolimus on revascularization have been poorly studied. Therefore, the current study investigated the effect of tacrolimus on islet revascularization using a highly sensitive imaging system and found, for the first time, that tacrolimus substantially abrogates revascularization of transplanted islet grafts.

The present study introduced a highly sensitive imaging system by combining the DSC technique and MPLSM in order to observe the time-dependent changes of newly-formed vessels surrounding the islet grafts [11]. This system allowed the

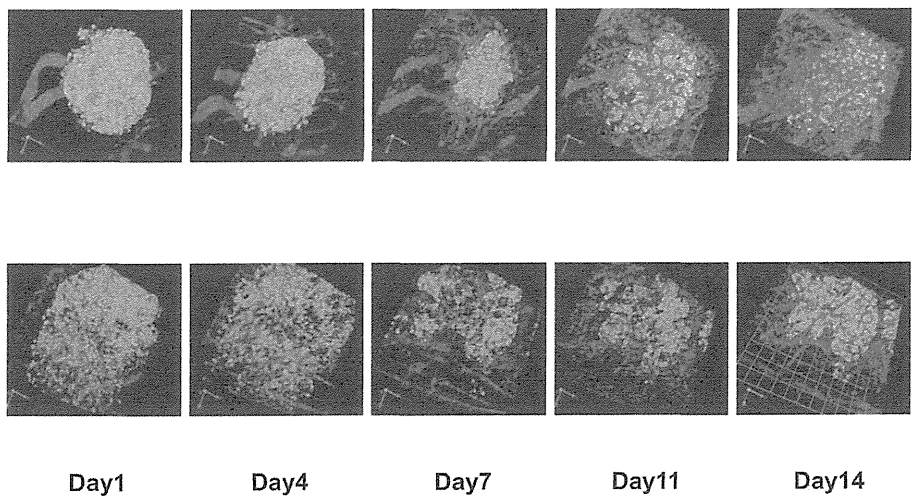

Figure 3. Imaging of the transplanted islets and surrounding blood vessels. Overlay of GFP fluorescence (pancreatic islets) and Texas Red fluorescence (blood vessels). Upper row: islets in the control group, Lower row: islets in the tacrolimus-treated group. GFP and Texas Red were excited at 890 nm. The scale bar indicated 51.0 μm/unit.
doi:10.1371/journal.pone.0056799.g003

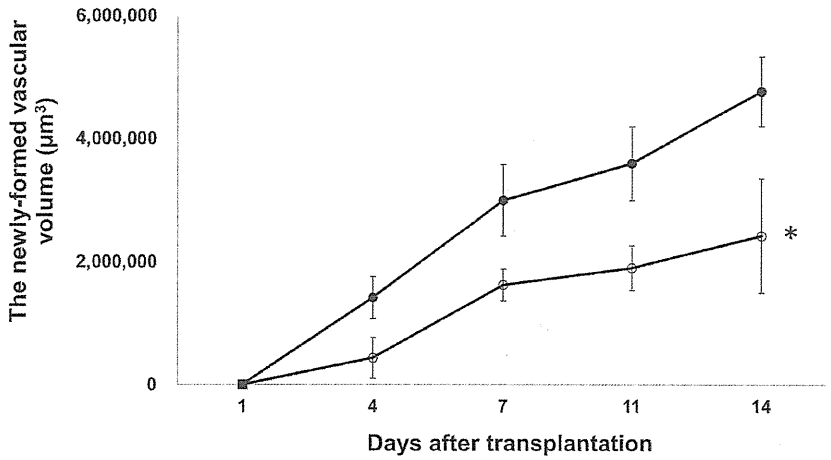

Figure 4. The time-dependent changes of newly-formed vascular volume surrounding the transplanted islets with and without tacrolimus. The newly-formed vascular volume in the control group (closed circles) and the tacrolimus-treated group (open circles). All values are expressed as the means ± SEM. *P<0.05 in comparison to the control group.
doi:10.1371/journal.pone.0056799.g004

observation of the same islet grafts repetitively in identical recipient animals without histological sectioning. Moreover, the use of athymic mice as recipients allowed the revascularization process to be monitored for a longer observation period. This system demonstrated that the revascularization process is completed within 14 days after pancreatic islet transplantation. This finding is consistent with several previous reports [24,25,26,27,28,29] performed by histological sectioning, thus indicating that this observation is accurate and also the established system was confirmed to be a useful tool to analyze the revascularization process of pancreatic islets.

This study further introduced the laser microdissection technique followed by real-time polymerase chain reaction (PCR) assay to analyze the state of gene expression in transplanted islet grafts *per se*. These combined methods using the highly sensitive imaging system and the laser microdissection technique together with real-time PCR assay allowed the simultaneous evaluation of the effect of immunosuppressive drugs not only on the revascularization process but also on the islet grafts *per se*. Notably, this elegant system could also be applicable for studying the angiogenesis and the engraftment in cancer cells and various stem cells.

The expression of *Vegfa*, *Mapk14*, *F3*, *Ccnd1* and *Cdk4* was suppressed in the islets transplanted without tacrolimus, in comparison to the islets prior to transplantation. However, unexpectedly, no difference was seen in hypoxia-inducible

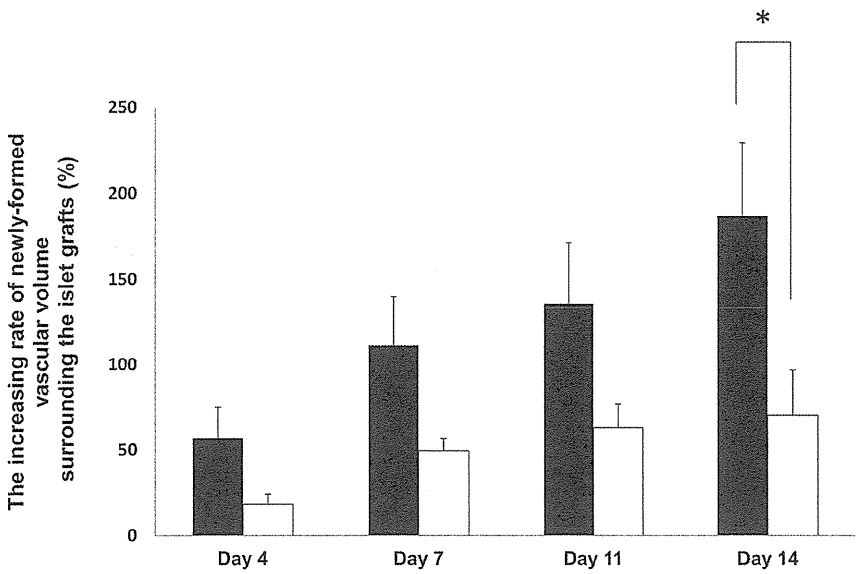

Figure 5. The increasing rate of newly-formed vascular volume surrounding the transplanted islets with and without tacrolimus. The increasing rate (against day 1) of newly-formed vascular volume surrounding the islets at 4, 7, 11, and 14 days after transplantation in the control group (black bar) and the tacrolimus-treated group (white bar) was calculated. All values are expressed as the means ± SEM. *P<0.05 in comparison to the control group.
doi:10.1371/journal.pone.0056799.g005

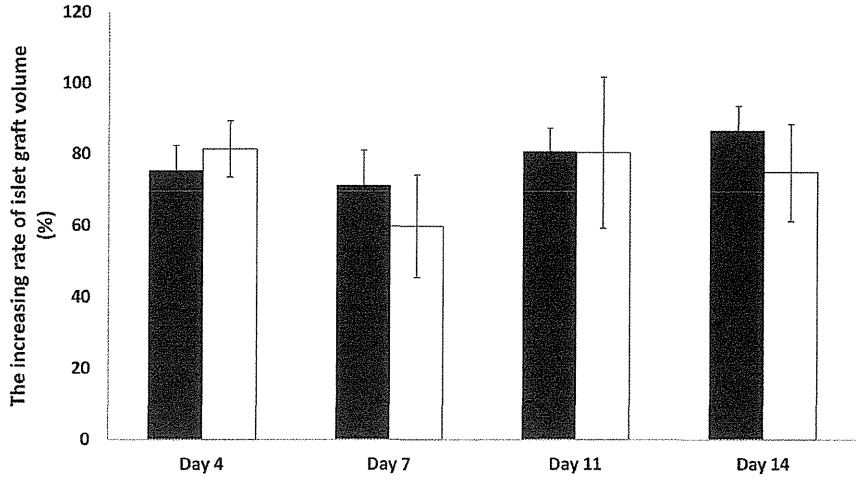

Figure 6. The increasing rate of islet graft volume with and without tacrolimus. The increasing rate (against day 1) of islet graft volume at 4, 7, 11, and 14 days after transplantation in the control group (black bar: n = 9) and the tacrolimus-treated group (white bar: n = 4) was calculated. All values are expressed as the means ± SEM.
doi:10.1371/journal.pone.0056799.g006

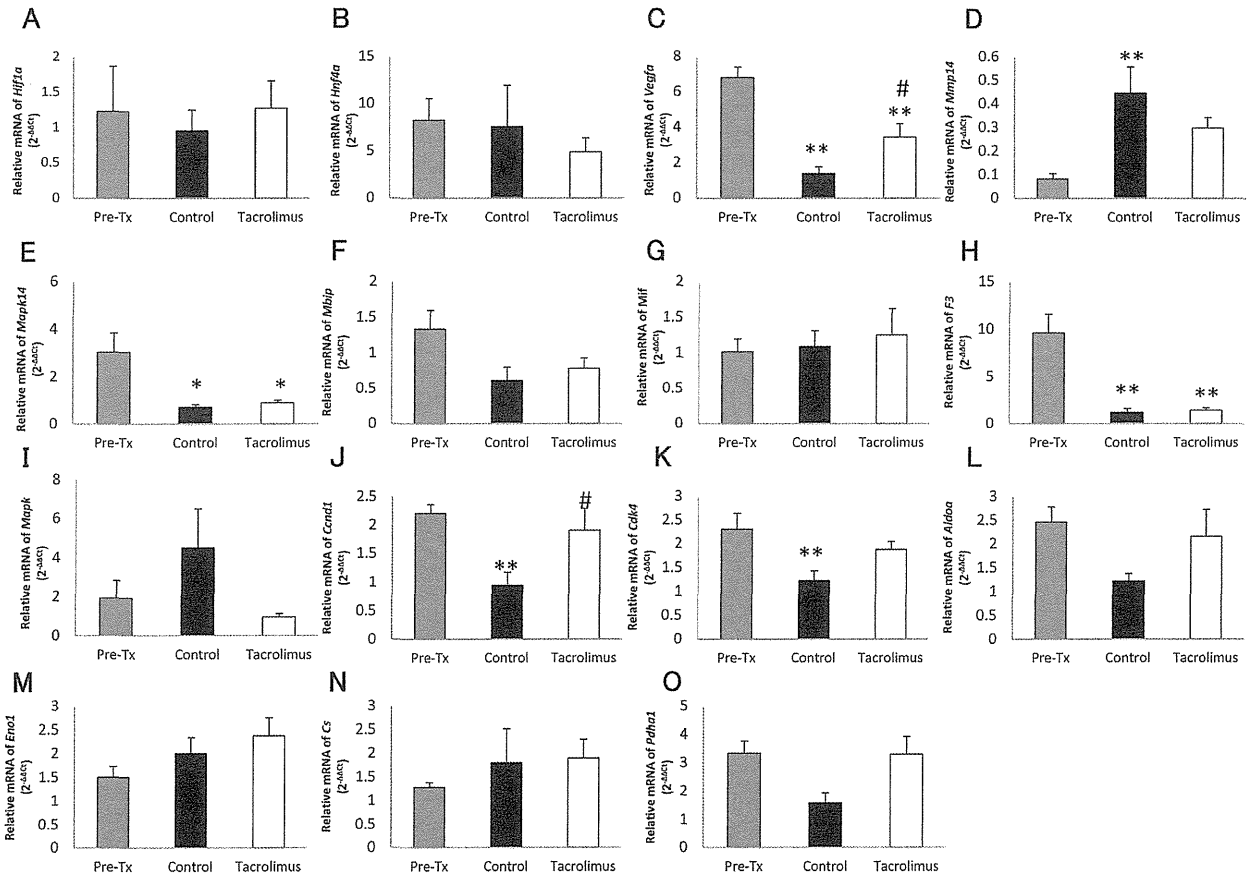

Figure 7. Relative gene expression in the transplanted pancreatic islets with and without tacrolimus. Relative gene expression of *Hif1a* (A), *Hnf4a* (B), *Vegfa* (C), *Mmp14* (D), *Mapk* (E), *Mbip* (F), *Mif* (G), *F3* (H),*Il1b* (I), *Ccnd1* (J), *Cdk4* (K), *AldoA* (L), *Eno1* (M), *Cs* (N), and *Pdha1* (O) in islets before transplantation (gray bar), the control group (black bar), and the tacrolimus-treated group (white bar). The values in the control and tacrolimus treated-group were represented as the ratio to the values in islets before transplantation. *P<0.05 in comparison to the islets before transplantation, **P<0.01 in comparison to the islets before transplantation, and #P<0.05 in comparison to the control group.
doi:10.1371/journal.pone.0056799.g007

factor-1α (*Hif1a*) which is induced by hypoxia. These data suggest that the subcutaneous space might not be as hypoxic as expected. One possible explanation is that only revascularized islets survived and were observed in the present study. Another possible explanation is that only a few islets were transplanted into the DSC, and thus there were enough spaces for angiogenesis surrounding the islet grafts.

The islets transplanted with tacrolimus showed a significantly different expression of *Vegfa* and ccnd1 in comparison to the islets transplanted without tacrolimus, but no differences were observed between the tacrolimus-treated and control groups in terms of other gene expression. Since the expression of *Vegfa*, which is a major stimulator of revascularization by inducing proliferation and migration of endothelial cells and tube formation [30,31,32], was upregulated, it could be speculated that a stimulator of revascularization such as transforming growth factor-β1 and macrophage-colony stimulating factor was released from transplanted islets in response to inhibition of revascularization induced by tacrolimus. However, *Mmp14*, which promotes angiogenesis through extracellular matrix degradation and improves revascularization of transplanted islets [33], was not upregulated in the present study, although Deryugina et al. have reported that *Mmp14* expression can be associated with an upregulation of *Vegf* production [34]. A possible explanation for this discrepancy might be a transplant model, but the detailed mechanism remains uncertain. Therefore, further investigations on the relevance of other growth factors derived from donor islets such as hepatocyte growth factor (HGF) and basic fibroblast growth factor (bFGF) [35,36] are also required in future studies. Considering that no suppression of analyzed gene expression and no reduction of islet graft volume were observed in the tacrolimus-treated group compared with the control group, the inhibitory effect of tacrolimus on islet revascularization may not be mediated by direct damage to the islet grafts. This also suggests a relatively lesser role for donor islet endothelial cells in revascularization process of islet grafts as shown by previous reports [27,37]. Although rapamycin was reported to have deleterious effects on islet viability and growth factor-induced cell cycle regulation [38,39], the present study suggests that tacrolimus appears to have no inhibitory effects on cell cycle regulation.

The dose of tacrolimus in the present study was determined according to previous studies. Lopez-Talavera et al. showed that the administration of tacrolimus at a dose of 0.5 mg/kg/day corresponds to a trough level of 6.0±1.5 ng/mL in rodents, which is similar to the dose used in the Edmonton protocol for humans [18]. Therefore, this dose was used for the tacrolimus-treated group. Islet revascularization was significantly inhibited after the administration of a clinical relevant dose of tacrolimus. Furthermore, Shapiro et al. reported that the portal C_{max} of immunosuppressive drugs was more than two times higher than the systemic C_{max} [40]. Therefore, the detrimental effect of tacrolimus on islet revascularization could be further enhanced when the islet grafts are transplanted into the liver, which is the current standard transplant site. As a result, the optimization of immunosuppressive drugs is of great importance for successful islet allotransplantation. FTY720, a sphingosine 1-phosphate analog, may be potentially useful and effective since previous studies have thus far shown it to effectively suppress immune responses in islet transplantation [41,42]. The established new evaluation system in the present study could be a useful screening tool for optimizing the protocols of revascularization including the immunosuppressive regimen.

In summary, the present study demonstrated that tacrolimus inhibits the revascularization of isolated pancreatic islets without affecting the characteristics of the transplanted grafts. Further refinements in this immunosuppressive regimen, especially with regard to the revascularization of islet grafts, could therefore improve the outcome of islet allotransplantation.

Supporting Information

Table S1 Genes analyzed for expression of transplanted islet grafts.
(DOCX)

Acknowledgments

The authors thank Megumi Goto, Toshiki Yanagi, and Masako Osawa for their excellent technical assistance. The authors also thank the Biomedical Research Core of Tohoku University Graduate School of Medicine for giving the opportunity to use MPLSM.

Author Contributions

Conceived and designed the experiments: RN MG. Performed the experiments: RN SN IF S. Sekiguchi KF AU MG. Analyzed the data: RN HS MS MG. Wrote the paper: RN TM NO S. Satomi MG.

References

1. Ryan EA, Paty BW, Senior PA, Bigam D, Alfadhli E, et al. (2005) Five-year follow-up after clinical islet transplantation. Diabetes 54: 2060–2069.
2. Sutherland DE, Gruessner AC, Carlson AM, Blondet JJ, Balamurugan AN, et al. (2008) Islet autotransplant outcomes after total pancreatectomy: a contrast to islet allograft outcomes. Transplantation 86: 1799–1802.
3. Goto M, Eich TM, Felldin M, Foss A, Kallen R, et al. (2004) Refinement of the automated method for human islet isolation and presentation of a closed system for in vitro islet culture. Transplantation 78: 1367–1375.
4. Goto M, Imura T, Inagaki A, Ogawa N, Yamaya H, et al. (2010) The impact of ischemic stress on the quality of isolated pancreatic islets. Transplant Proc 42: 2040–2042.
5. Shapiro AM, Lakey JR, Ryan EA, Korbutt GS, Toth E, et al. (2000) Islet transplantation in seven patients with type 1 diabetes mellitus using a glucocorticoid-free immunosuppressive regimen. N Engl J Med 343: 230–238.
6. Zhang N, Su D, Qu S, Tse T, Bottino R, et al. (2006) Sirolimus is associated with reduced islet engraftment and impaired beta-cell function. Diabetes 55: 2429–2436.
7. Guba M, von Breitenbuch P, Steinbauer M, Koehl G, Flegel S, et al. (2002) Rapamycin inhibits primary and metastatic tumor growth by antiangiogenesis: involvement of vascular endothelial growth factor. Nat Med 8: 128–135.
8. Stallone G, Schena A, Infante B, Di Paolo S, Loverre A, et al. (2005) Sirolimus for Kaposi's sarcoma in renal-transplant recipients. N Engl J Med 352: 1317–1323.
9. Cantaluppi V, Biancone L, Romanazzi GM, Figliolini F, Beltramo S, et al. (2006) Antiangiogenic and immunomodulatory effects of rapamycin on islet endothelium: relevance for islet transplantation. Am J Transplant 6: 2601–2611.
10. Turgut B, Guler M, Akpolat N, Demir T, Celiker U (2011) The impact of tacrolimus on vascular endothelial growth factor in experimental corneal neovascularization. Curr Eye Res 36: 34–40.
11. Nishimura R, Goto M, Sekiguchi S, Fujimori K, Ushiyama A, et al. (2011) Assessment for revascularization of transplanted pancreatic islets at subcutaneous site in mice with a highly sensitive imaging system. Transplant Proc 43: 3239–3240.
12. Speier S, Nyqvist D, Cabrera O, Yu J, Molano RD, et al. (2008) Noninvasive in vivo imaging of pancreatic islet cell biology. Nat Med 14: 574–578.
13. Speier S, Nyqvist D, Kohler M, Caicedo A, Leibiger IB, et al. (2008) Noninvasive high-resolution in vivo imaging of cell biology in the anterior chamber of the mouse eye. Nat Protoc 3: 1278–1286.
14. Goto M, Johansson H, Maeda A, Elgue G, Korsgren O, et al. (2004) Low molecular weight dextran sulfate prevents the instant blood-mediated inflammatory reaction induced by adult porcine islets. Transplantation 77: 741–747.
15. Goto M, Tjernberg J, Dufrane D, Elgue G, Brandhorst D, et al. (2008) Dissecting the instant blood-mediated inflammatory reaction in islet xenotransplantation. Xenotransplantation 15: 225–234.
16. Bayne K (1996) Revised Guide for the Care and Use of Laboratory Animals available. American Physiological Society. Physiologist 39: 199, 208–111.

17. Ushiyama A, Yamada S, Ohkubo C (2004) Microcirculatory parameters measured in subcutaneous tissue of the mouse using a novel dorsal skinfold chamber. Microvasc Res 68: 147–152.
18. Lopez-Talavera JC, Garcia-Ocana A, Sipula I, Takane KK, Cozar-Castellano I, et al. (2004) Hepatocyte growth factor gene therapy for pancreatic islets in diabetes: reducing the minimal islet transplant mass required in a glucocorticoid-free rat model of allogeneic portal vein islet transplantation. Endocrinology 145: 467–474.
19. Mita A, Ricordi C, Messinger S, Miki A, Misawa R, et al. (2010) Antiproinflammatory effects of iodixanol (OptiPrep)-based density gradient purification on human islet preparations. Cell Transplant 19: 1537–1546.
20. Goto M, Eich TM, Stahle M, Malmborg A, Engkvist M, et al. (2005) Technical improvement of human pancreatic islet isolation. Transplant Proc 37: 1313–1314.
21. Ichii H, Pileggi A, Molano RD, Baidal DA, Khan A, et al. (2005) Rescue purification maximizes the use of human islet preparations for transplantation. Am J Transplant 5: 21–30.
22. Reffet S, Thivolet C (2006) Immunology of pancreatic islet transplantation. Diabetes Metab 32: 523–526.
23. Singh RP, Stratta RJ (2008) Advances in immunosuppression for pancreas transplantation. Curr Opin Organ Transplant 13: 79–84.
24. Menger MD, Yamauchi J, Vollmar B (2001) Revascularization and microcirculation of freely grafted islets of Langerhans. World J Surg 25: 509–515.
25. Vajkoczy P, Olofsson AM, Lehr HA, Leiderer R, Hammersen F, et al. (1995) Histogenesis and ultrastructure of pancreatic islet graft microvasculature. Evidence for graft revascularization by endothelial cells of host origin. Am J Pathol 146: 1397–1405.
26. Sandberg JO, Margulis B, Jansson L, Karlsten R, Korsgren O (1995) Transplantation of fetal porcine pancreas to diabetic or normoglycemic nude mice. Evidence of a rapid engraftment process demonstrated by blood flow and heat shock protein 70 measurements. Transplantation 59: 1665–1669.
27. Andersson A, Korsgren O, Jansson L (1989) Intraportally transplanted pancreatic islets revascularized from hepatic arterial system. Diabetes 38 Suppl 1: 192–195.
28. Merchant FA, Diller KR, Aggarwal SJ, Bovik AC (1997) Angiogenesis in cultured and cryopreserved pancreatic islet grafts. Transplantation 63: 1652–1660.
29. Mendola JF, Goity C, Fernandez-Alvarez J, Saenz A, Benarroch G, et al. (1994) Immunocytochemical study of pancreatic islet revascularization in islet isograft. Effect of hyperglycemia of the recipient and of in vitro culture of islets. Transplantation 57: 725–730.
30. Lai Y, Schneider D, Kidszun A, Hauck-Schmalenberger I, Breier G, et al. (2005) Vascular endothelial growth factor increases functional beta-cell mass by improvement of angiogenesis of isolated human and murine pancreatic islets. Transplantation 79: 1530–1536.
31. Zhang N, Richter A, Suriawinata J, Harbaran S, Altomonte J, et al. (2004) Elevated vascular endothelial growth factor production in islets improves islet graft vascularization. Diabetes 53: 963–970.
32. Johansson A, Olerud J, Johansson M, Carlsson PO (2009) Angiostatic factors normally restrict islet endothelial cell proliferation and migration: implications for islet transplantation. Transpl Int 22: 1182–1188.
33. Olsson R, Maxhuni A, Carlsson PO (2006) Revascularization of transplanted pancreatic islets following culture with stimulators of angiogenesis. Transplantation 82: 340–347.
34. Deryugina EI, Soroceanu L, Strongin AY (2002) Up-regulation of vascular endothelial growth factor by membrane-type 1 matrix metalloproteinase stimulates human glioma xenograft growth and angiogenesis. Cancer Res 62: 580–588.
35. Vasir B, Reitz P, Xu G, Sharma A, Bonner-Weir S, et al. (2000) Effects of diabetes and hypoxia on gene markers of angiogenesis (HGF, cMET, uPA and uPAR, TGF-alpha, TGF-beta, bFGF and Vimentin) in cultured and transplanted rat islets. Diabetologia 43: 763–772.
36. Watanabe H, Sumi S, Kitamura Y, Nio Y, Higami T (2003) Immunohistochemical analysis of vascular endothelial growth factor and hepatocyte growth factor, and their receptors, in transplanted islets in rats. Surg Today 33: 854–860.
37. Henriksnas J, Lau J, Zang G, Berggren PO, Kohler M, et al. (2012) Markedly decreased blood perfusion of pancreatic islets transplanted intraportally into the liver: disruption of islet integrity necessary for islet revascularization. Diabetes 61: 665–673.
38. Aronovitz A, Josefson J, Fisher A, Newman M, Hughes E, et al. (2008) Rapamycin inhibits growth factor-induced cell cycle regulation in pancreatic beta cells. J Investig Med 56: 985–996.
39. Cross SE, Richards SK, Clark A, Benest AV, Bates DO, et al. (2007) Vascular endothelial growth factor as a survival factor for human islets: effect of immunosuppressive drugs. Diabetologia 50: 1423–1432.
40. Shapiro AM, Gallant HL, Hao EG, Lakey JR, McCready T, et al. (2005) The portal immunosuppressive storm: relevance to islet transplantation? Ther Drug Monit 27: 35–37.
41. Maeda A, Goto M, Zhang J, Bennet W, Groth CG, et al. (2003) Immunosuppression with FTY720 and cyclosporine A inhibits rejection of adult porcine islet xenografts in rats. Transplantation 75: 1409–1414.
42. Shapiro AM, Lakey JR, Paty BW, Senior PA, Bigam DL, et al. (2005) Strategic opportunities in clinical islet transplantation. Transplantation 79: 1304–1307.

Solution Structure of Clostridial Collagenase H and Its Calcium-Dependent Global Conformation Change

Naomi Ohbayashi,[†‡] Takashi Matsumoto,[§] Hiroki Shima,[¶] Masafumi Goto,[¶‖] Kimiko Watanabe,[‖] Akihito Yamano,[§] Yasutake Katoh,[¶] Kazuhiko Igarashi,[¶] Youhei Yamagata,[**] and Kazutaka Murayama[†*]

[†]Graduate School of Biomedical Engineering, Tohoku University, Sendai, Japan; [‡]Faculty of Pharmacy, Iwaki Meisei University, Iwaki, Japan; [§]Rigaku Corporation, Akishima, Japan; [¶]Graduate School of Medicine, Tohoku University, Sendai, Japan; [‖]New Industry Creation Hatchery Center, Tohoku University, Sendai, Japan; and [**]Graduate School of Agricultural Science, Tokyo University of Agriculture and Technology, Tokyo, Japan

ABSTRACT Collagenase H (ColH) from *Clostridium histolyticum* is a multimodular protein composed of a collagenase module (activator and peptidase domains), two polycystic kidney disease-like domains, and a collagen-binding domain. The interdomain conformation and its changes are very important for understanding the functions of ColH. In this study, small angle x-ray scattering and limited proteolysis were employed to reveal the interdomain arrangement of ColH in solution. The ab initio beads model indicated that ColH adopted a tapered shape with a swollen head. Under calcium-chelated conditions (with EGTA), the overall structure was further elongated. The rigid body model indicated that the closed form of the collagenase module was preferred in solution. The limited proteolysis demonstrated that the protease sensitivity of ColH was significantly increased under the calcium-chelated conditions, and that the digestion mainly occurred in the domain linker regions. Fluorescence measurements with a fluorescent dye were performed with the limited proteolysis products after separation. The results indicated that the limited proteolysis products exhibited fluorescence similar to that of the full-length ColH. These findings suggested that the conformation of full-length ColH in solution is the elongated form, and this form is calcium-dependently maintained at the domain linker regions.

INTRODUCTION

Clostridial collagenases are multimodular proteins consisting of three to five domains. The collagenases commonly contain a collagenase module, which is composed of activator and peptidase domains, at the N-terminal side and a collagen-binding domain (CBD) at the C-terminal end (1) (Fig. 1). Among the five collagenases, the collagenase from *Clostridium histolyticum*, ColH, has only one CBD, whereas the collagenase from *Clostridium botulinum*, ColB, possesses three CBDs. The other three collagenases, ColG from *C. histolyticum*, ColA from *Clostridium perfringens*, and ColT from *Clostridium tetani*, include two CBDs. Although ColT only consists of these two domain and module types (collagenase module and CBD), the other collagenases, except for ColH, include a polycystic kidney disease (PKD)-like domain, which may be involved in collagen recruitment (2). ColH includes two PKD-like domains, PKD1 and PKD2 (Fig. 1).

Intensive structural analyses of the individual domains of ColG and ColH have been conducted. The first crystal structure was reported for the CBD of ColG (3). The CBD structures were solved with calcium ions (holo form) and without calcium ions (apo form). The crystal structure of the collagenase module of ColG was recently determined (4) and revealed that bacterial collagenolysis proceeds by a chew-and-digest mechanism, in which the structural changes of the collagenase module, were suggested to involve open and closed conformations. Although a structural analysis was performed for the region from Tyr-119 to Gly-790, containing the collagenase module and the PKD-like domain, the position of the PKD-like domain was not exactly located in the crystal structure (4). The structure of the PKD-like domain was determined and discussed by the same group in a subsequent report (2). In addition to these structures, the crystal structures of the CBD of ColH have been deposited in the Protein Data Bank (PDB-IDs: 3JQW and 3JQX) (5). The sequence identities among the individual domains of ColH and ColG were calculated using ClustalW (6). The results showed that they are well conserved: 48% for the collagenase modules; 40–50% for the PKD-like domains; and 29–34% for the CBDs.

Calcium ions play a critical role in the enhancement of the interactions between collagens and collagenases (7,8). Furthermore, the binding mode of the CBD to the collagen triple-helix was proposed, based on NMR titration and small angle x-ray scattering (SAXS) studies (3,9). Ca^{2+} ion binding to collagenases contributes to the interactions with collagen and the stability of the CBD (3,10). In addition, Ca^{2+} ions reportedly play very important roles in the interdomain flexibility and thermal stability of full-length ColH, and are reversibly regulated (11).

The molecular mechanisms of the individual domains of collagenases have been investigated, in terms of both their structures and functions. However, the structure of

Submitted August 25, 2012, and accepted for publication February 14, 2013.

*Correspondence: kmura@bme.tohoku.ac.jp

Editor: Lois Pollack.

© 2013 by the Biophysical Society

0006-3495/13/04/1538/8 $2.00

http://dx.doi.org/10.1016/j.bpj.2013.02.022

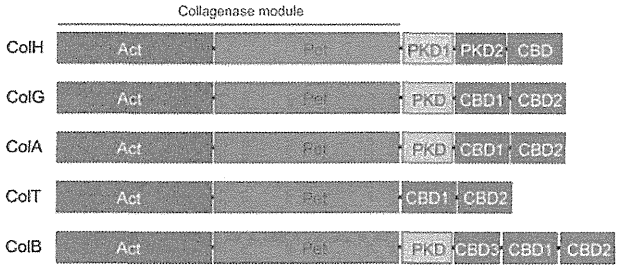

FIGURE 1 Domain architectures of clostridial collagenases. The five collagenases are ColH and ColG of *C. histolyticum*, ColA of *C. perfringens*, ColT of *C. tetani*, and ColB of *C. botulinum*. The domain notations are Act, activator domain; Pet, peptidase domain; PKD, polycystic kidney disease-like domain; CBD, collagen-binding domain.

the collagenase molecule, as a multidomain protein, remains poorly characterized. Here, we report the structural characterization of full-length ColH in solution. For the structural analysis of biological macromolecules in solution, SAXS is an important and useful approach (12–15). The ab initio beads model of ColH indicated that the overall conformation adopted a tapered form, with the longest dimension of ~140 Å. Under calcium-chelated conditions (with EGTA), the structure was further elongated. A limited proteolysis analysis indicated that the sensitivity to the protease was significantly increased under the calcium-chelated conditions. Fluorescence measurements suggested that a calcium-dependent conformational change occurred in the collagenase module. To our knowledge, this is the first investigation of the solution structure of full-length ColH and its calcium-dependent conformational change.

MATERIALS AND METHODS

Protein expression and purification

The protein sample was prepared as previously described (11). Briefly, ColH was expressed in *Escherichia coli* strain BL21(DE3) as a secreted form, and was subsequently purified using a Ni-NTA superflow (Qiagen, Hilden, Germany) column. The eluted protein was then subjected to MonoQ and Superdex 200 gel filtration chromatography (GE Healthcare, Little Chalfont, United Kingdom). The peak fractions were pooled and concentrated in 20 mM HEPES buffer (pH 8.0), containing 100 mM NaCl and 1 mM $CaCl_2$, to a final concentration of 11.0 mg/mL.

SAXS measurements

SAXS data were collected using a BioSAXS-1000 system equipped with an FR-E+ rotating anode x-ray generator (Rigaku, Akishima, Japan). The protein samples were prepared at concentrations of 1, 5, and 10 mg/mL with a calcium-containing buffer, and 10 mg/mL with a buffer containing 2 mM EGTA. The wavelength, λ, was 1.54189 Å (CuKα), and the sample-detector distance was 500 mm, leading to scattering vectors, q, that ranged from 0.009 to 0.65 $Å^{-1}$ with $q = (4\pi/\lambda)\sin\theta$, where 2θ is the scattering angle. The protein solutions or buffer (30 μL) were placed in a quartz capillary with a diameter of 1.0 mm, and the exposure time was 15 min/frame. The total exposure times for the calcium-containing conditions were 120 min for the 5 and 10 mg/mL solutions, and 240 min for the 1 mg/mL solution. For the EGTA-containing conditions, the total exposure times were 180, 240, and 360 min for the 10, 5, and 2 mg/mL solutions, respectively. The scattering images were processed with SAXSLab installed in the BioSAXS system (Rigaku), and the scattering intensities from the buffer solution were subtracted with PRIMUS (16). The forward scattering, $I(0)$, and the radius of gyration, R_g, were estimated using the Guinier approximation in the ATSAS program package (17). The $P(r)$ distributions were calculated from the scattering data for the 10 mg/mL solution with GNOM (18), by applying perceptual criteria for the estimation of D_{max}.

Ab initio and rigid body modeling

Ab initio modeling of the scattering envelopes was performed with GASBOR (19). The calculated resolution range was $0.009 < q < 0.60$ $Å^{-1}$. Eight individual reconstructions were calculated and averaged using DAMAVER (20). ColH domain models were prepared by SWISS-MODEL (21), using the crystal structures of ColG (collagenase module: 2Y3U; PKD-like domain: 3JS7) as the templates, except for the CBD. For the model of the CBD, PDB-ID: 3JQW was used. The closed conformation model for the collagenase module was manually built, as proposed in the collagen processing model (4), before homology modeling by SWISS-MODEL. Whole rigid body model construction was conducted for the ab initio beads model under the conditions with calcium, using these individual domain models. Before the BUNCH calculation, the domain models were aligned sequentially from the collagenase module to the CBD, with appropriate distances corresponding to the missing amino acids in the domain linker regions. The final ColH model was constructed by BUNCH (22) in the User mode with scattering data of $q < 0.2$, and was corrected manually. During the BUNCH calculations, distance restraints were used (2–3 Å/missing amino acid in the initial models). The theoretical scattering curve from the final model was calculated by CRYSOL (23). The ColH model was fitted to the beads model by SUPCOMB (24).

Limited proteolysis and electrospray ionization mass spectrometry

A ColH solution (1 mg/mL) was prepared in 20 mM HEPES (pH 8.0), 100 mM NaCl, 1 mM $CaCl_2$, in the presence or absence of 2 mM EGTA. Limited proteolysis was performed with lysyl endopeptidase (Lys-C; Sigma, St. Louis, MO) at an enzyme/substrate ratio of 1:200 (w/w) at 30°C. In the time course experiments, Lys-C proteolysis was stopped at 0, 2, 6, 10, 20, and 30 min by the addition of phenylmethylsulfonyl fluoride (final concentration, 1 mM). For the C-terminal fragment analysis, the ColH solution was digested by Lys-C for 30 min at 30°C as described previously, and then treated with carboxypeptidase B (16 units/mL) for 10 min at 30°C. The partially hydrolyzed products were separated by sodium dodecyl sulfate-polyacrylamide gel electrophoresis (SDS-PAGE). The bands on the SDS-PAGE gel were excised, placed in individual sample tubes, and subjected to in-gel trypsin digestion for 20 h at 37°C. The digested peptides were loaded onto a 75-μm fused silica capillary column containing C18 resin. The peptides were eluted with an acetonitrile gradient (typically 2.5–40%) in 0.1% formic acid, and analyzed by an LTQ Orbitrap XL mass spectrometer (Thermo Fisher Scientific, Waltham, MA).

Size exclusion chromatography and fluorescence measurements of the limited proteolysis products

A ColH solution (11 mg/mL) with 2 mM EGTA was hydrolyzed by Lys-C at 1:1,000 (w/w) at 30°C for 60 min. The partially hydrolyzed products were separated by size exclusion chromatography on a Superdex 200 column (GE Healthcare). The buffer conditions were the same as those in the purification process. The fractions containing the protein corresponding to the

100-kDa band on the SDS-PAGE gel were pooled and reapplied to the Superdex 200 column, to estimate the molecular mass under two different buffer conditions (with and without 2 mM EGTA). To prepare the 80 kDa band protein, a ColH solution was hydrolyzed as described previously, although for 180 min. The hydrolyzed products were separated by ion-exchange chromatography (ResourceQ, GE Healthcare) to purify the 80 kDa band protein. The fluorescence of both partially hydrolyzed products (100 and 80 kDa band proteins) was measured using an F-2500 spectrofluorometer (Hitachi, Tokyo, Japan) at 25°C. Fluorescence spectra were measured with an excitation wavelength of 492 nm, with emission from 500 to 650 nm. The excitation and emission bandwidths were both set at 10 nm. The ColH samples were mixed with freshly diluted SYPRO Orange (Invitrogen, Carlsbad, CA) (1:1000, v/v) under three different conditions: 1), with intact buffer; 2), with 2 mM EGTA; and 3), with additional 2 mM $CaCl_2$ added after 2 mM EGTA. The measurements were performed three times.

RESULTS

Overall conformation of ColH

To evaluate the overall structure, ColH was subjected to a SAXS analysis in the calcium-containing buffer (buffer-Ca: 20 mM HEPES (pH 8.0), 100 mM NaCl, and 1 mM $CaCl_2$) and buffer-Ca with 2 mM EGTA (buffer-Ca/EGTA: 20 mM HEPES (pH 8.0), 100 mM NaCl, 1 mM $CaCl_2$, and 2mM EGTA) (Fig. 2 *a*). The free Ca^{2+} concentration in the buffer-Ca/EGTA was estimated as 3.95 nM (pCa 8.4) by CHELATOR (25). Protein aggregation complicates the interpretation of scattering curves. The ratios of the forward scattering intensity to the concentration ($I(0)/c$) were comparable for the three concentrations (1 (or 2), 5, and 10 mg/mL) with buffer-Ca and buffer-Ca/EGTA (Table 1), suggesting that concentration or time-dependent aggregation did not occur. The SAXS analysis provides two important parameters for evaluating molecular size in solution: the radius of gyration, R_g, as the mean molecular size; and the maximal intermolecular dimension, D_{max}. The Guinier plots indicated that R_g was 37.9 Å in buffer-Ca and 39.1 Å in buffer-Ca/EGTA (Fig. 2 *b*). The $P(r)$ distributions were estimated by an indirect Fourier transformation of the intensity data (Fig. 2 *c*). The D_{max} values were calculated to be 138 Å in buffer-Ca and 184 Å in buffer-Ca/EGTA, from the $P(r)$ profile of ColH. Both SAXS parameters were increased by calcium chelation with EGTA. The low resolution ab initio model building was conducted using GASBOR (19). Fig. 3 *a* shows the ab initio beads models in buffer-Ca and buffer-Ca/EGTA. Under both buffer conditions, the overall shape of ColH was an elongated form with a swollen head region that tapered off toward the end. The longest dimension of ColH was further extended by calcium chelation with EGTA, as shown in the calculation of D_{max}. The dimensions of the swollen head regions were estimated to be ~90 × 45 Å and 70 × 70 Å in buffer-Ca and buffer-Ca/EGTA, respectively. On the other hand, the widths of the tapered end were 20–30 Å under both conditions.

Rigid body model construction fitted to SAXS data

To construct the domain arrangement of ColH, the known structures of the individual domains of clostridial collagenases were used. The rigid body model was built using homology-modeled structures (collagenase module (activator and peptidase domains) and two PKD-like domains of ColG) and the CBD of ColH. The crystal structure of the ColG collagenase module is the open form (4). However, the conformation of the open form did not fit the beads model of ColH in buffer-Ca, because the width of the open form of the collagenase module is ~115 Å, whereas that of the beads model is 90 Å. The approximate dimensions of the closed form of the collagenase domain are 85 × 60 Å, which fit the beads model dimensions well (Fig. 4 *a*). Considering the two structural variations of the collagenase module, the closed form of the collagenase module was adopted for modeling. The final rigid body model fit well to the beads model in buffer-Ca (Fig. 4 *b*). The modeled structure lacked structural information for the domain linker regions. These regions were Gly-721 to Ser-726 (between the peptidase domain and

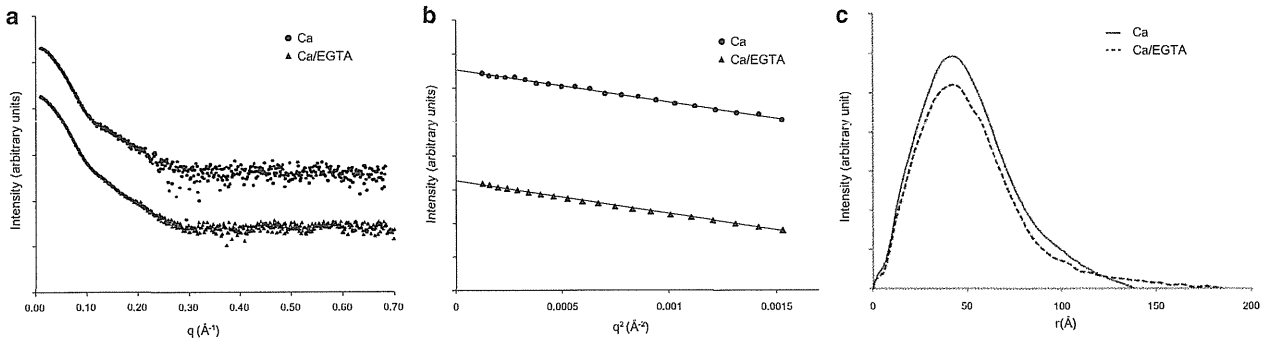

FIGURE 2 SAXS experiments. (*a*) Scattering data of ColH. The plots were vertically translated for clarity. (*b*) Guinier plot of a 10 mg/mL solution of ColH. The triangles and squares indicate the plots in buffer-Ca and buffer-Ca/EGTA, respectively. The plots were vertically translated for clarity. (*c*) Distance distribution functions, $P(r)$, for ColH in buffer-Ca (*solid line*) and buffer-Ca/EGTA (*dashed line*).

TABLE 1 Overall SAXS parameters

Protein concentration	Guinier analysis	Indirect Fourier transformation			
c, mg/ml	R_g, Å	D_{max}, Å	R_g, Å	$I(0)$	$I(0)$/c
(Buffer-Ca)					
10	37.9 ± 0.5	138	39.2 ± 0.2	2.164 ± 0.01	0.216
5	37.2 ± 0.8	138	39.5 ± 0.4	1.109 ± 0.009	0.222
1	36.5 ± 1.1	130	37.2 ± 0.5	0.203 ± 0.003	0.203
(Buffer-Ca/EGTA)					
10	39.1 ± 0.1	184	41.4 ± 0.3	1.900 ± 0.004	0.190
5	39.1 ± 0.2	184	41.4 ± 0.4	0.954 ± 0.003	0.191
2	39.8 ± 0.4	184	44.8 ± 0.5	0.403 ± 0.003	0.202

the first PKD-like domain), Leu-811 to Lys-815 (between the first PKD-like domain and the second PKD-like domain), and Pro-901 to Val-902 (between the second PKD-like domain and the CBD). The domain linker regions were relatively short (see Fig. S1 in the Supporting Material). Therefore, each domain was able to contact the adjacent domain. Although the crystal structures of the full-length clostridial collagenases have not been solved, an entire model of ColG on collagen microfibrils has been proposed (2,4). A comparison of these models revealed the similarity between the overall structural characteristics.

The beads model in buffer-Ca/EGTA was a further elongated form. A conformational change induced by calcium chelation has been reported for the CBD of ColG (3,10) and full-length ColH (11). Superposition of the rigid body model in buffer-Ca and the beads model in buffer-Ca/EGTA revealed that an unfitted region existed around the collagenase module and the CBD (Fig. 3 *b*), suggesting its conformational change by the calcium chelation.

Cleavage sites in limited proteolysis

Limited proteolysis is a useful tool for detecting protein flexibility (26). The sensitivity to protease digestion differs significantly between folded regions and unfolded regions, such as flexible loops. In this study, Lys-C was used as the protease for the limited proteolysis analysis, because it is specific for lysine residues, which are distributed throughout the ColH sequence. This residue-specific protease has the advantage of producing homogeneous ends in the digested peptide fragments, and these homogeneous ends facilitate subsequent analyses because of the reduced variation in the fragments.

Protease digestion was hardly observed for ColH in buffer-Ca. In contrast, ColH in buffer-Ca/EGTA was rapidly digested into three main bands, as evaluated by SDS-PAGE (Fig. 5 *a*). To determine the cleavage sites, fragment analyses by mass spectrometry were performed, by calculating the ratio of the detected fragment number from the limited proteolysis to the nondigested protein. The plot of the ratio should be reduced to zero when the limited proteolysis products do not include the N- and/or C-terminal regions. The results revealed that the three main bands were fragments digested at the C-terminal region. The evaluated C-terminal ends were Lys-915, Lys-825, and Lys-724, respectively (Fig. S2). In the second band, some additional fragments were detected, with digestion positions at 872–881. The limited proteolysis products treated with carboxypeptidase B provided a fragment without the C-terminal lysine. Therefore, the fragment at the C-terminal end is a semitryptic fragment. Such fragments were also detected for the first and third bands on SDS-PAGE in Fig. 5 *a*, but not for the second band (Fig. S1). Consequently, the sites digested by Lys-C mainly correspond to the domain linker regions between the second PKD-like domain and the

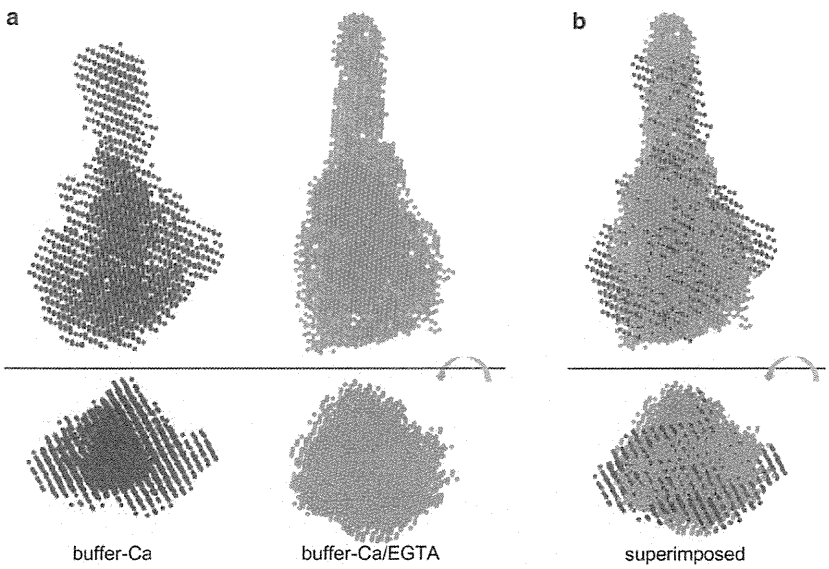

FIGURE 3 Comparison of the two ab initio beads models. (*a*) The beads models are represented in cyan for buffer-Ca and pink for buffer-Ca/EGTA. (*b*) A superimposed model with the beads models depicted in the same colors as in panel (*a*).

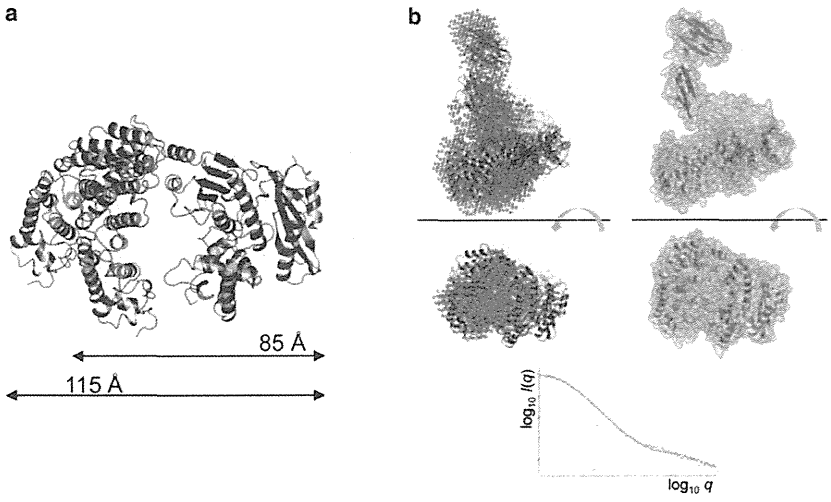

FIGURE 4 Model fitting between the ab initio beads model and the rigid body model. (*a*) Superimposed collagenase module conformations. The two conformations are superimposed on the peptidase domain. The activator domains of the conformations are colored blue (*solid*) and green (*open*). (*b*) Superimposition between the beads model in buffer-Ca and the rigid body model. (*Upper left panel*) The rigid body model is drawn as a ribbon representation and colored blue (collagenase module), yellow (PKD-like domain 1), magenta (PKD-like domain 2), and green (CBD). (*Upper right panel*) Surface representation of the rigid body model. (*Lower panel*) Evaluation of the modeled structure. The theoretical scattering curve was fitted to the SAXS data (*dots*).

CBD (Lys-915; ColHΔCBD) for the first band, the first PKD-like domain and the second PKD-like domain (Lys-825; ColHΔPKD-CBD) for the second band, and the collagenase module and the first PKD-like domain (Lys-724; ColHΔPKD-PKD-CBD) for the third band. According to the time course of the digestion pattern, the linker region between the second PKD-like domain and the CBD was clearly and significantly sensitive to digestion. On the other hand, the linker region between the first PKD-like domain and the second PKD-like domain was barely digested.

Analyses of the limited proteolysis products

The limited proteolysis products included three different domain-deleted ColH products, ColHΔPKD-PKD-CBD, ColHΔPKD-CBD, and ColHΔCBD. Among these products, ColHΔPKD-PKD-CBD and ColHΔCBD were purified by size exclusion chromatography (Fig. 5 *b*). Size exclusion chromatography of the purified ColHΔCBD revealed different elution volumes between the running buffers, i.e., 14.06 mL with buffer-Ca and 13.87 mL with buffer-Ca/EGTA (Fig. 5 *c*).

ColH reportedly shows fluorescence with the dye SYPRO Orange under the calcium-chelated conditions (11). This observation suggested that the interdomain conformation of ColH can be stabilized by hydrophobic interactions, because a fluorescent dye like SYPRO Orange binds to hydrophobic regions on the molecular surface (27). Fluorescence measurements were conducted for the fractions eluted from the size exclusion chromatography, to investigate the shortened domain constructions of ColH. The fluorescence enhancements of ColHΔCBD and ColHΔPKD-PKD-CBD were similar to that of the full-length protein (Fig. 5 *d*).

DISCUSSION

The crystal structure of the collagenase module of ColG was determined as the open form (4). The longest dimension of the collagenase module spans 115 Å, which is too wide to fit the beads models under both buffer conditions (buffer-Ca and buffer-Ca/EGTA), assuming the proposed domain alignment (4). Considering reasonable model dimensions, the closed form was adopted to fit the beads model. The collagenase module is composed of activator and peptidase domains, and these two domains are connected by a flexible glycine-rich hinge in ColG. No special secondary structural element was assigned for the corresponding part in ColH in the PSIPred (28) analysis. Therefore, the linker region between the activator domain and the peptidase domain of ColH is probably flexible. The closed form may be more stable than the open form in solution, because the N-terminal part of the activator domain and the putative loop region between Ser-529 and Phe-535 of the peptidase domain can interact. Consequently, the collagenase module of ColH predominantly adopts the closed form in solution.

The SAXS analysis revealed that ColH adopted a tapered shape under both conditions; i.e., in buffer-Ca and buffer-Ca/EGTA. In a comparison of the two beads models, the beads model in buffer-Ca/EGTA was more elongated (Fig. 3). Calcium ions reportedly play a critical role in maintaining the conformation of full-length ColH (11). In addition, the details of the calcium-dependent structural change have been reported for the CBDs of ColG (3,10,29) and ColH (5). The crystal structure of the CBD of ColH has also been determined for the calcium-binding form (PDB-ID: 3JQW) (5). The calcium-binding sites are spatially shared in both CBDs, suggesting that the calcium-dependent structural change of the CBD of ColH can occur in the same manner as that of ColG. According to the limited proteolysis analysis, the first digestion occurred at position Lys-915, which is the domain linker region between the second PKD-like domain and the CBD. The results suggested that the shape elongation of full-length ColH in buffer-Ca/EGTA includes a structural

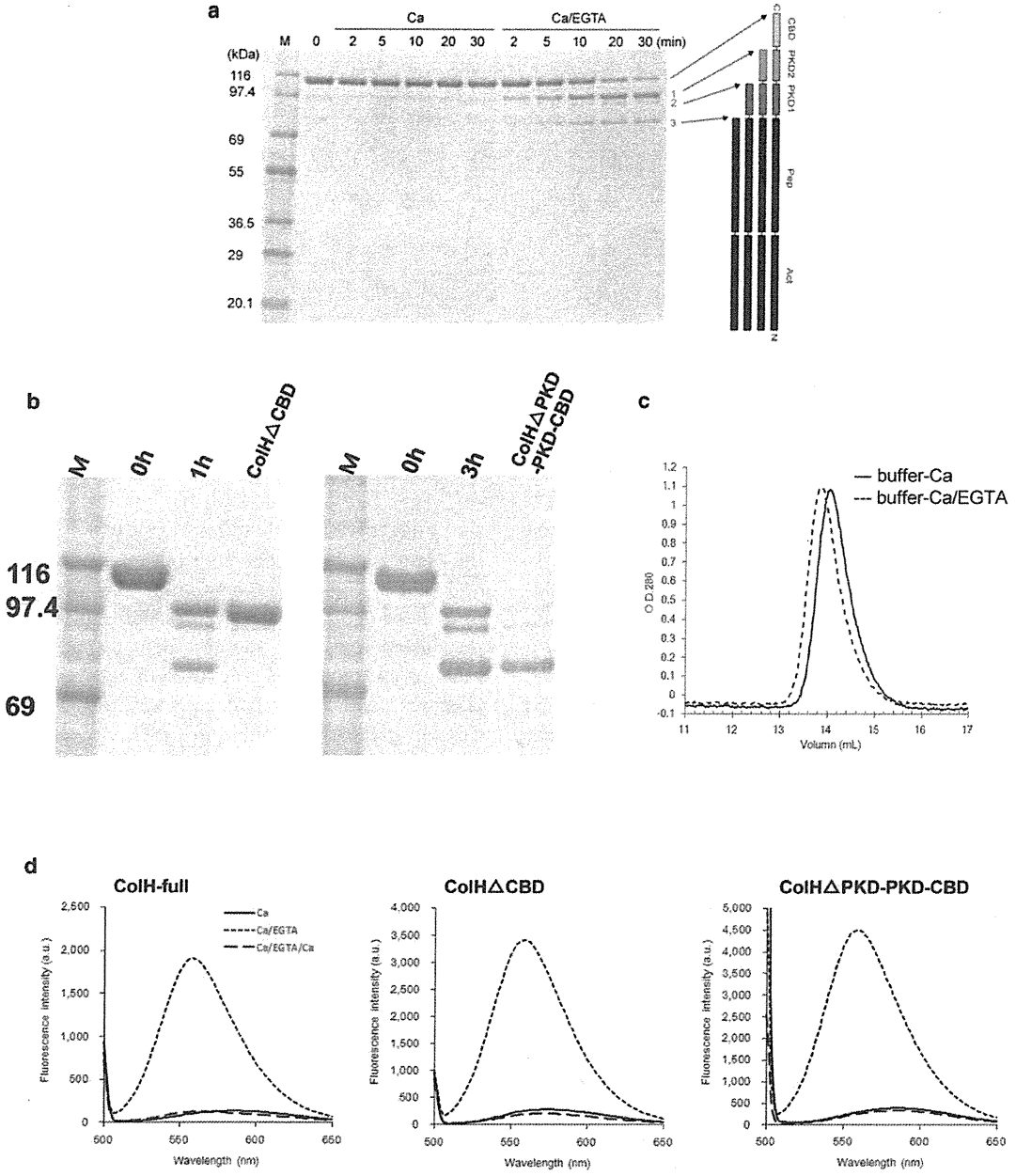

FIGURE 5 Limited proteolysis analyses. (*a*) SDS-PAGE analysis of the time course of the limited proteolysis products. The presumed C-terminal positions are indicated by arrows. M: protein standard markers. (*b*) SDS-PAGE of two limited proteolysis products. (*c*) Size exclusion chromatography of the C-terminal-deleted product ColHΔCBD under the two buffer conditions. (*d*) Fluorescence measurements of the limited proteolysis products. Solid line: without protein; long dashed line: in buffer-Ca/EGTA; short dashed line: after the addition of 2 mM $CaCl_2$ to the buffer-Ca/EGTA (buffer-Ca/EGTA/Ca). Left panel: full-length ColH; middle panel: C-terminal-deleted product, ColHΔCBD; right panel: C-terminal-deleted product, ColHΔPKD-PKD-CBD.

change at the linker region between the second PKD-like domain and the CBD.

The size exclusion chromatography analysis of ColHΔCBD indicated that the elution peak position with calcium was later than that with EGTA. This phenomenon was also found for the elution volumes of full-length ColH (11). The conformational change induced by calcium chelation with EGTA may reduce the interactions between the protein molecules and the matrix of the chromatography column, suggesting a calcium-dependent structural change of ColHΔCBD.

The limited proteolysis products were separated, and fluorescence measurements with the dye SYPRO Orange were conducted for the C-terminal-deleted products,

ColHΔPKD-PKD-CBD and ColHΔCBD. The separated C-terminal-deleted products showed similar fluorescence enhancement to that of full-length ColH. ColHΔPKD-PKD-CBD is identical to the collagenase module, and its calcium-dependent fluorescence is reversibly changed by the addition of excess calcium ions after calcium-chelation by EGTA. Fluorescence with a dye like SYPRO Orange indicates the existence of hydrophobic interactions (27). These results suggested that the ColH molecule without the CBD and the PKD-like domains; i.e., the collagenase module, includes calcium-binding site(s), and that its conformation may be maintained by hydrophobic interactions and calcium ion(s). Actually, about five calcium ions can bind to the entire ColH region (30). Two calcium ions are assigned to the CBD (3), and one ion is expected to bind to the PKD-like domain (2). Thus, at least four calcium ion-binding sites can be assigned on the ColH molecule to date. The fluorescence measurements indicated the possibility of a calcium-dependent conformational change in the collagenase module. Although it is difficult to explain how the conformation of the collagenase module changes upon calcium chelation, open/closed changes are one of the possibilities, because the crystal structure of the ColG collagenase module-PKD was determined under conditions without calcium (4).

CONCLUSIONS

In this study, a SAXS analysis was conducted to investigate the structural basis of the conformational change of full-length ColH induced by calcium chelation. The overall conformation of ColH is the tapered form under both buffer conditions. Although the crystal structure of the collagenase module of ColG is the open form, the collagenase module of ColH in solution with calcium predominantly adopts the closed form. The closed form will be more stable, as a consequence of interdomain interactions between the activator domain and the peptidase domain in solution.

We previously reported that the interdomain flexibility is predominantly and reversibly maintained by Ca^{2+} (11). In a comparison of the ab initio beads models under the two conditions (with buffer-Ca and buffer-Ca/EGTA), a more elongated structure was observed under the calcium-chelated conditions. The main conformational change will occur in the domain linker regions, especially the linker region between the second PKD-like domain and the CBD. The analysis of the limited proteolysis products suggested that the conformation of the collagenase module can be maintained in a calcium-dependent manner. Although the calcium-binding site on the collagenase module has not been determined thus far, further studies will be undertaken to investigate the molecular mechanism of the conformational change of the collagenase module.

SUPPORTING MATERIAL

Two supplemental figures and their legends are available at http://www.biophysj.org/biophysj/supplemental/S0006-3495(13)00239-7.

We acknowledge the support of the Biomedical Research Core of Tohoku University, Graduate School of Medicine, and TAMRIC (Tohoku Advanced Medical Research and Incubation Center).

This research was supported in part by the Coordination, Support and Training Program for Translational Research from the Ministry of Education, Culture, Sports, Science and Technology, Japan.

REFERENCES

1. Bruggemann, H., S. Baumer, ..., G. Gottschalk. 2003. The genome sequence of *Clostridium tetani*, the causative agent of tetanus disease. *Proc. Natl. Acad. Sci. USA.* 100:1316–1321.
2. Eckhard, U., and H. Brandstetter. 2011. Polycystic kidney disease-like domains of clostridial collagenases and their role in collagen recruitment. *Biol. Chem.* 392:1039–1045.
3. Wilson, J. J., O. Matsushita, ..., J. Sakon. 2003. A bacterial collagen-binding domain with novel calcium-binding motif controls domain orientation. *EMBO J.* 22:1743–1752.
4. Eckhard, U., E. Schönauer, ..., H. Brandstetter. 2011. Structure of collagenase G reveals a chew-and-digest mechanism of bacterial collagenolysis. *Nat. Struct. Mol. Biol.* 18:1109–1114.
5. Bauer, R., J. J. Wilson, ..., J. Sakon. 2013. Structural comparison of ColH and ColG collagen-binding domains from *Clostridium histolyticum*. *J. Bacteriol.* 195:318–327.
6. Thompson, J. D., D. G. Higgins, and T. J. Gibson. 1994. CLUSTAL W: improving the sensitivity of progressive multiple sequence alignment through sequence weighting, position-specific gap penalties and weight matrix choice. *Nucleic Acids Res.* 22:4673–4680.
7. Matsushita, O., C. M. Jung, ..., A. Okabe. 1998. A study of the collagen-binding domain of a 116-kDa *Clostridium histolyticum* collagenase. *J. Biol. Chem.* 273:3643–3648.
8. Matsushita, O., T. Koide, ..., A. Okabe. 2001. Substrate recognition by the collagen-binding domain of *Clostridium histolyticum* class I collagenase. *J. Biol. Chem.* 276:8761–8770.
9. Philominathan, S. T., T. Koide, ..., J. Sakon. 2009. Unidirectional binding of clostridial collagenase to triple helical substrates. *J. Biol. Chem.* 284:10868–10876.
10. Philominathan, S. T., O. Matsushita, ..., J. Sakon. 2009. Ca2+-induced linker transformation leads to a compact and rigid collagen-binding domain of *Clostridium histolyticum* collagenase. *FEBS J.* 276:3589–3601.
11. Ohbayashi, N., N. Yamagata, ..., K. Murayama. 2012. Enhancement of the structural stability of full-length clostridial collagenase by calcium ions. *Appl. Environ. Microbiol.* 78:5839–5844.
12. Jacques, D. A., and J. Trewhella. 2010. Small-angle scattering for structural biology–expanding the frontier while avoiding the pitfalls. *Protein Sci.* 19:642–657.
13. Mertens, H. D., and D. I. Svergun. 2010. Structural characterization of proteins and complexes using small-angle X-ray solution scattering. *J. Struct. Biol.* 172:128–141.
14. Svergun, D. I. 2010. Small-angle X-ray and neutron scattering as a tool for structural systems biology. *Biol. Chem.* 391:737–743.
15. Schneidman-Duhovny, D., S. J. Kim, and A. Sali. 2012. Integrative structural modeling with small angle X-ray scattering profiles. *BMC Struct. Biol.* 12:17.
16. Konarev, P. V., V. V. Volkov, ..., D. I. Svergun. 2003. PRIMUS: a Windows PC-based system for small-angle scattering data analysis. *J. Appl. Cryst.* 36:1277–1282.

17. Petoukhov, M. V., P. V. Konarev, ..., D. I. Svergun. 2007. ATSAS 2.1 - towards automated and web-supported small-angle scattering data analysis. *J. Appl. Cryst.* 40:S223–S228.

18. Svergun, D. I. 1992. Determination of the regularization parameter in indirect-transform methods using perceptual criteria. *J. Appl. Cryst.* 25:495–503.

19. Svergun, D. I., M. V. Petoukhov, and M. H. J. Koch. 2001. Determination of domain structure of proteins from X-ray solution scattering. *Biophys. J.* 80:2946–2953.

20. Volkov, V. V., and D. I. Svergun. 2003. Uniqueness of ab initio shape determination in small-angle scattering. *J. Appl. Cryst.* 36:860–864.

21. Arnold, K., L. Bordoli, ..., T. Schwede. 2006. The SWISS-MODEL workspace: a web-based environment for protein structure homology modelling. *Bioinformatics.* 22:195–201.

22. Petoukhov, M. V., and D. I. Svergun. 2005. Global rigid body modeling of macromolecular complexes against small-angle scattering data. *Biophys. J.* 89:1237–1250.

23. Svergun, D., C. Barberato, and M. H. J. Koch. 1995. CRYSOL - a program to evaluate x-ray solution scattering of biological macromolecules from atomic coordinates. *J. Appl. Cryst.* 28:768–773.

24. Kozin, M. B., and D. I. Svergun. 2001. Automated matching of high- and low-resolution structural models. *J. Appl. Cryst.* 34:33–41.

25. Schoenmakers, T. J., G. J. Visser, ..., A. P. Theuvenet. 1992. CHELATOR: an improved method for computing metal ion concentrations in physiological solutions. *Biotechniques.* 12:870–874, 876–879.

26. Dokudovskaya, S., R. Williams, ..., M. P. Rout. 2006. Protease accessibility laddering: a proteomic tool for probing protein structure. *Structure.* 14:653–660.

27. Epps, D. E., and B. M. Taylor. 2001. A competitive fluorescence assay to measure the reactivity of compounds. *Anal. Biochem.* 295:101–106.

28. Buchan, D. W. A., S. M. Ward, ..., D. T. Jones. 2010. Protein annotation and modelling servers at University College London. *Nucleic Acids Res.* 38(Web Server issue):W563–W568.

29. Sides, C. R., R. Liyanage, ..., J. Sakon. 2012. Probing the 3-D structure, dynamics, and stability of bacterial collagenase collagen binding domain (apo- versus holo-) by limited proteolysis MALDI-TOF MS. *J. Am. Soc. Mass Spectrom.* 23:505–519.

30. Bond, M. D., and H. E. Van Wart. 1984. Characterization of the individual collagenases from *Clostridium histolyticum. Biochemistry.* 23:3085–3091.

2. Orlando G, Soker S, Wood K. Operational tolerance after liver transplantation [review]. *J Hepatol* 2009; 50: 1247.
3. Roussey-Kesler G, Giral M, Moreau A, et al. Clinical operational tolerance after kidney transplantation. *Am J Transplant* 2006; 6: 736.
4. Brouard S, Pallier A, Renaudin K, et al. The natural history of clinical operational tolerance after kidney transplantation through twenty-seven cases. *Am J Transplant* 2012; 12: 3296.
5. Waldmann H. Tolerance: an overview and perspectives [review]. *Nat Rev Nephrol* 2010; 6: 569.
6. Jovanovic V, Lair D, Soulillou JP, et al. Transfer of tolerance to heart and kidney allografts in the rat model. *Transpl Int* 2008; 21: 199.
7. Girlanda R, Kirk AD. Frontiers in nephrology: immune tolerance to allografts in humans. *J Am Soc Nephrol* 2007; 18: 2242.
8. Pallier A, Hillion S, Danger R, et al. Patients with drug-free long-term graft function display increased numbers of peripheral B cells with a memory and inhibitory phenotype. *Kidney Int* 2010; 78: 503.
9. Brouard S, Mansfield E, Braud C, et al. Identification of a peripheral blood transcriptional biomarker panel associated with operational renal allograft tolerance. *Proc Natl Acad Sci U S A* 2007; 104: 15448.
10. Sagoo P, Perucha E, Sawitzki B, et al. Development of a cross-platform biomarker signature to detect renal transplant tolerance in humans. *J Clin Invest* 2010; 120: 1848.
11. Newell KA, Asare A, Kirk AD, et al. Identification of a B cell signature associated with renal transplant tolerance in humans. *J Clin Invest* 2010; 120: 1836.
12. Giral M, Foucher Y, Karam G, et al. Kidney and recipient weight incompatibility reduces long-term graft survival. *J Am Soc Nephrol* 2010; 21: 1022.
13. Haynes L, Jankowska-Gan E, Sheka A, et al. Donor-specific indirect pathway analysis reveals a B-cell-independent signature which reflects outcomes in kidney transplant recipients. *Am J Transplant* 2012; 12: 640.
14. Louis S, Braudeau C, Giral M, et al. Contrasting $CD25^{hi}CD4^{+}$ T cells/FOXP3 patterns in chronic rejection and operational drug-free tolerance. *Transplantation* 2006; 81: 398.
15. Andreola G, Chittenden M, Shaffer J, et al. Mechanisms of donor-specific tolerance in recipients of haploidentical combined bone marrow/kidney transplantation. *Am J Transplant* 2011; 11: 1236.
16. Miqueu P, Guillet M, Degauque N, et al. Statistical analysis of CDR3 length distributions for the assessment of T and B cell repertoire biases. *Mol Immunol* 2007; 44: 1057.
17. Danger R, Pallier A, Giral M, et al. Upregulation of miR-142-3p in peripheral blood mononuclear cells of operationally tolerant patients with a renal transplant. *J Am Soc Nephrol* 2012; 23: 597.
18. Lozano JJ, Pallier A, Martinez-Llordella M, et al. Comparison of transcriptional and blood cell-phenotypic markers between operationally tolerant liver and kidney recipients. *Am J Transplant* 2011; 11: 1916.
19. Deng S, Moore DJ, Huang X, et al. Cutting edge: transplant tolerance induced by anti-CD45RB requires B lymphocytes. *J Immunol* 2007; 178: 6028.
20. Huang X, Moore DJ, Mohiuddin M, et al. Inhibition of ICAM-1/LFA-1 interactions prevents B-cell-dependent anti-CD45RB-induced transplantation tolerance. *Transplantation* 2008; 85: 675.
21. Zhao G, Moore DJ, Lee KM, et al. An unexpected counter regulatory role of IL10 in B lymphocyte mediated transplantation tolerance. *Am J Transplant* 2010; 10: 796.
22. Ueno T, Habicht A, Clarkson MR, et al. The emerging role of T cell Ig mucin 1 in alloimmune responses in an experimental mouse transplant model. *J Clin Invest* 2008; 118: 742.
23. Ding Q, Yeung M, Camirand G, et al. Regulatory B cells are identified by expression of TIM-1 and can be induced through TIM-1 ligation to promote tolerance in mice. *J Clin Invest* 2011; 121; 3645.
24. Le Texier L, Thebault P, Lavault A, et al. Long-term allograft tolerance is characterized by the accumulation of B cells exhibiting an inhibited profile. *Am J Transplant* 2011; 11: 429.
25. Terasaki PI. Humoral theory of transplantation. *Am J Transplant* 2003; 3: 665.
26. Colvin RB. Antibody-mediated renal allograft rejection: diagnosis and pathogenesis. *J Am Soc Nephrol* 2007; 18: 1046.
27. Ballet C, Roussey-Kesler G, Aubin JT, et al. Humoral and cellular responses to influenza vaccination in human recipients naturally tolerant to a kidney allograft. *Am J Transplant* 2006; 6: 2796.
28. Sachs D, Sykes M, Kawai T, et al. Immunointervention for the induction of transplantation tolerance through mixed chimerism [review]. *Semin Immunol* 2011; 23: 165.

Clinical Experiences in the Treatment of Pancreatic Arteriovenous Malformation by Total Pancreatectomy With Islet Autotransplantation

Pancreatic arteriovenous malformation (AVM) is defined as a tumorous formation or vascular anomaly that builds up via an aberrant bypass anastomosis of the arterial and venous systems in the pancreas (Fig. 1A) (*1*). Most AVM cases have pancreatic bleeding due to portal hypertension and the rupture of abnormal vessels (*2, 3*), and AVM is thought to correlate with pancreatitis (*2*). AVM may be an indication for surgical therapy, including total pancreatectomy (TP). To prevent diabetes induced by TP, islet autotransplantation (IAT) can be an ideal choice.

Three male AVM patients underwent TP with IAT at our institute. Their ages were 39, 52, and 59 years. All had had one or more attacks of pancreatitis. Pancreatic pseudocysts were found in the body or tail of the pancreas in all three patients, and all of them had had episodes of bleeding in the pseudocyst. Patients 1 and 2 underwent emergency TP with IAT due to bleeding. We selected a two-step procedure for the TPs (distal pancreatectomy and pancreaticoduodenectomy), because TP for AVM presents a risk of massive bleeding. The warm ischemic times were within 10 min in all three patients, and the cold ischemia times were 33 (body/tail) and 74 min (head) in patient 1, 52 (body/tail) and 81 min (head) in patient 2, and 32 (body/tail) and 197 min (head) in patient 3. The numbers of isolated islets and total tissue volume were 355,270 islet equivalents (IEQ) and 5.7 mL (patient 1), 244,758 IEQ and 16.0 mL (patient 2), and 310,238 IEQ and 1.0 mL (patient 3). The percentages of purity were 30% to 60% (patient 1), 15% to 40% (patient 2), and 40% to 80% (patient 3).

Many larger clusters derived from a cystic lesion were detected in patient 2. There was no increase or only a slight increase in the portal vein pressure and no adverse events during transplantation, except in patient 2 (it was significantly increased to 26 mm Hg). Thus, we had to stop patient 2's transplantation when half of the islets were transplanted, but severe hypoglycemia occurred during and after transplantation. No recurrence has been seen thus far at the transplanted site in any of the patients.

Figure 1B shows the preoperative and postoperative courses of the patients. The blood glucose levels were well controlled using low-dose insulin injection in

Copyright © 2013 Lippincott Williams & Wilkins. Unauthorized reproduction of this article is prohibited.

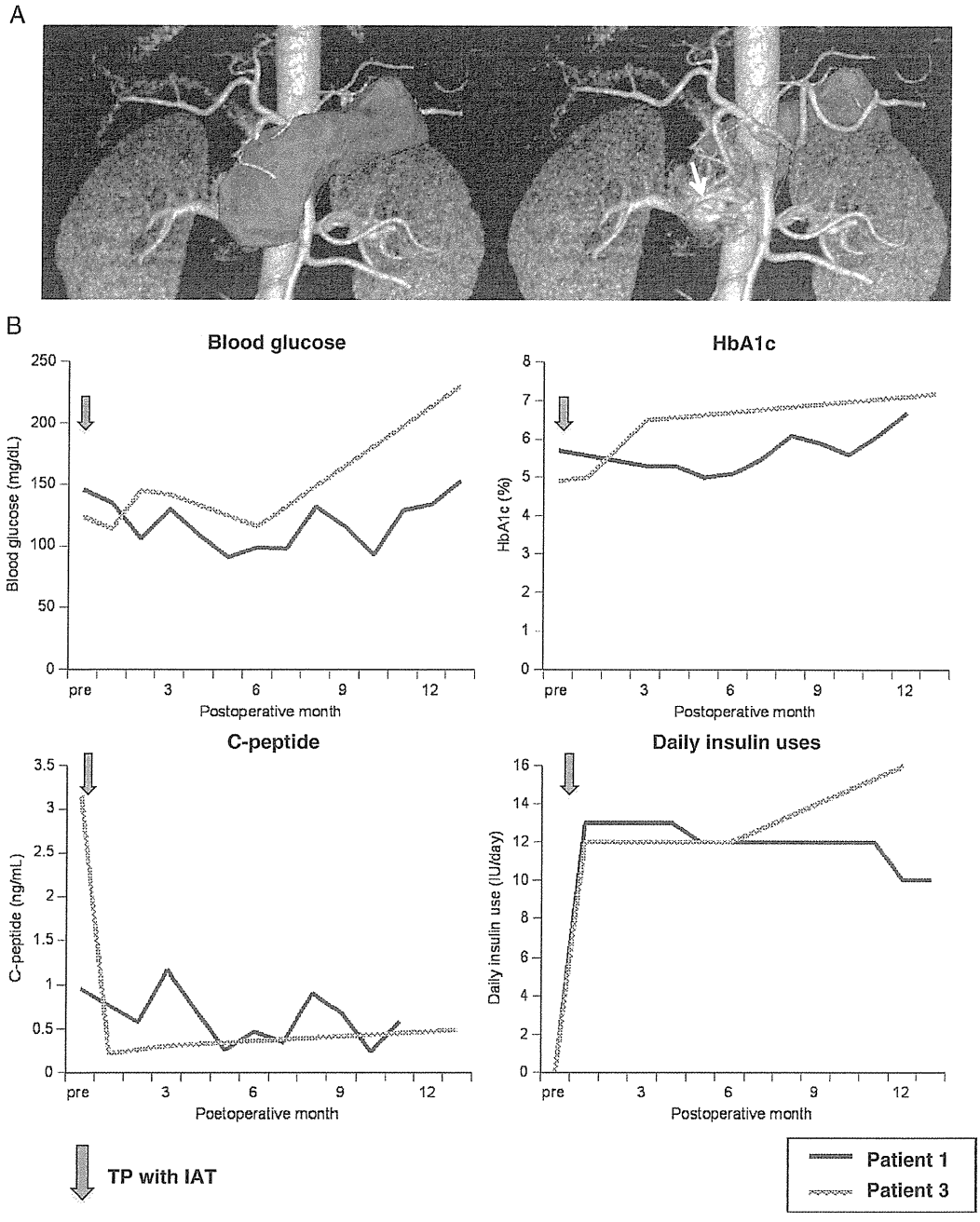

FIGURE 1. A, abdominal 3D (left, opacification; right, rarefaction) computed tomography imaging of an AVM patient. Conglomerations of small vessels were detected around and in the pancreas (arrow). B, blood glucose, HbA1c, serum C-peptide, and daily insulin use changes before and after TP with IAT in patients 1 and 3. The blood glucose levels were well controlled by a low-dose insulin injection in these patients. The blood glucose of the recipients was well maintained without hypoglycemia, and a substantial level of fasting C-peptide was observed under a low dose of daily insulin supplementation.

patients 1 and 3. The blood glucose of the recipients was well maintained without hypoglycemia, and a substantial level of fasting C-peptide was observed under a low dose of daily insulin supplementation. The secretory unit of islet in transplantation indexes, calculated as 250×(fasting C-peptide [nM])/(fasting blood glucose [nM]-3.43) (*4*), were 15 to 27 in patient 1 and 6 to 10 in patient 3. These two patients were free from severe and uncontrollable diabetes mellitus. Patient 2 had severe adverse events and poor control of blood glucose. He had total portal thrombus on day 1 after transplantation, and an emergency surgery was performed due to liver dysfunction caused by the portal thrombus. The portal vein thrombectomy was done, and then anticoagulant therapy by continuous injection of heparin and urokinase was performed. Finally, the blood flow in the portal vein recovered and the elevated hepatic enzymes were improved. He was discharged on 92 days after transplantation, but his blood glucose levels became unstable (they increased to >300 mg/dL).

Copyright © 2013 Lippincott Williams & Wilkins. Unauthorized reproduction of this article is prohibited.